

Entanglement from superradiance and rotating quantum fluids of light

Adrià Delhom,^{1,*} Killian Guerrero,² Paula Calizaya,¹ Kévin Falque,²
Anthony J. Brady,^{3,4} Ivan Agullo,¹ and Maxime J. Jacquet^{2,†}

¹*Department of Physics and Astronomy, Louisiana State University, Baton Rouge, LA 70803, U.S.A.*

²*Laboratoire Kastler Brossel, Sorbonne Université, CNRS, ENS-Université PSL,
Collège de France, 4 Place Jussieu, Paris, 75005, France.*

³*Department of Electrical and Computer Engineering,
University of Arizona, Tucson, Arizona 85721, USA*

⁴*Ming Hsieh Department of Electrical and Computer Engineering,
University of Southern California, Los Angeles, California 90089, USA*

The amplification of radiation by superradiance is a universal phenomenon observed in numerous physical systems. We demonstrate that superradiant scattering generates entanglement for different input states, including coherent states, thereby revealing the inherently quantum nature of this phenomenon. To put these concepts to the test, we propose a novel approach to create horizonless ergoregions, which are nonetheless dynamically stable thanks to the dissipative dynamics of a polaritonic fluid of light. We numerically simulate the system to demonstrate the creation of a stable ergoregion, and experimentally realize a comparable configuration. Subsequently, we investigate rotational superradiance within this system, with a primary focus on entanglement generation and the possibilities for its enhancement using current techniques. Our methods permit the investigation of quantum emission by rotational superradiance by controlling the input state at will.

I. INTRODUCTION

Superradiance describes the amplification of radiation by time-independent potentials, a phenomenon that occurs across a broad spectrum of systems, including optics [1], fluid dynamics [2], electrodynamics [3–5], particle physics [6, 7], and fields on curved spacetimes relativity [2, 8–12].

Rotational superradiance [2, 13] occurs in spinning systems featuring an ergoregion — a region within which material bodies are dragged around and forced to co-rotate with the system (see [14] for a review).¹ While all bodies have positive energy outside the ergoregion, frame dragging permits the existence of bodies with negative energies within. The mixing of positive- and negative-energies across the boundary of the ergoregion (the ergosurface) allows for incoming waves to be reflected with larger amplitudes.

The availability of negative energy states implies a quantum instability [2, 13, 15, 16], by which the vacuum decays into pairs of field excitations. This entails the unavoidable presence of a finite population of excitations inside the ergosurface. If this population is not dissipated away by some mechanism, it will be further amplified by superradiance, leading to an instability. Ergoregions are thus intrinsically unstable [17].

In known stable configurations, dissipation is provided by a horizon inside the ergosurface (as, for instance, in spinning black holes). A horizon is a one-way membrane, which effectively dissipates negative energy modes out of

the system. However, horizons emit Hawking radiation, meaning that ergosurfaces are constantly exposed to an energy flux from the horizon. In other words, the input state of rotational superradiance in such configurations is never the vacuum, but thermal Hawking radiation instead. This has prevented the isolation of quantum emission solely due to rotational superradiance.

In studies of superradiance, a coherent state is typically employed to externally illuminate the ergoregion (see, e.g., [14]). The ensuing emission statistics are dominated by classical amplitudes, vastly surpassing the contributions from vacuum emission, including emissions from the horizon. Any potential quantum effects produced in the emission, such as entanglement, get lost among classical data (noise, classical correlations etc.). For this reason, superradiance is commonly understood as a classical amplification phenomenon.

This is the context within which rotational superradiance has been investigated experimentally [18, 19]. In these experiments, the focus was on observing the reflection of the incoming coherent state. Energy conservation demands that the observed amplified wave is accompanied by a partner negative energy excitation in the ergoregion. However, experimental limitations were such that negative energy waves were not observed, and neither were correlations across the ergosurface.

This paper focuses on quantum emission by superradiance. On the one hand, we show how superradiance generates entanglement for a variety of input states, establishing it as an entanglement-generating phenomenon. On the other hand, we propose a new experimental setup to test our theoretical findings, involving the creation of horizonless configurations with an ergoregion that is nevertheless stable. We use a two-dimensional quantum fluid of light made of microcavity polaritons (hybrid particles made of a photon and an electric dipole) with intrinsic

* adria.delhom@gmail.com

† maxime.jacquet@lkb.upmc.fr

¹ This is different from Dicke superradiance that describes the collective amplification of radiation by coherent emitters [1].

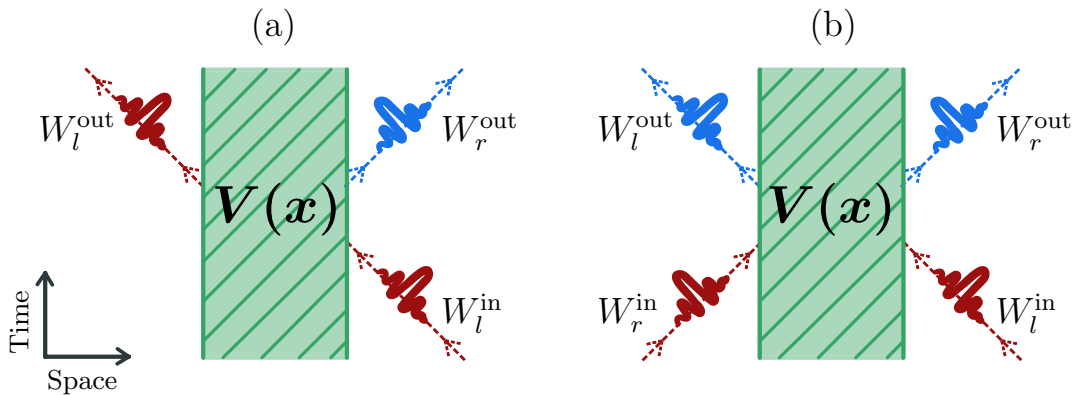


FIG. 1. Illustration of wave packet scattering by a time-independent potential. (a) An incoming left-moving wave packet scatters into an outgoing left-moving (transmitted) wave packet and a right-moving wave packet (reflected). (b) General scattering with incoming modes approaching the potential from both sides.

cally dissipative dynamics, using this to our advantage to control the ergoregion instability while minimizing data loss. We experimentally create an irrotational vortex featuring an ergosurface. This experimental realization is complemented by numerical simulations of the polariton dynamics indicating the occurrence of rotational superradiance in that configuration.

The ability to create isolated ergoregions is promising, as it permits the investigation of the properties of super-radiant emission by controlling the input state at will. Observing entanglement generated in pair-production processes has remained a challenge. We argue that the ability of ergoregions to amplify entanglement combined with the unique capabilities of fluids of light offer a promising avenue to achieve this benchmark. This article lays the theoretical groundwork and presents experimental progress toward the observation of entanglement from rotational superradiance.

II. SUPERRADIANT WAVE SCATTERING IN A NUTSHELL

Superradiant scattering occurs when the transmission and/or reflection coefficients of a stationary potential exceed unity. In such cases, the amplitudes of the scattered waves are larger than that of the incident wave, at the expense of the potential, which supplies the necessary energy for the amplification process to occur.

Our objective in this section is to delineate the conditions under which superradiance universally occurs, and pinpoint the key mechanisms behind it. To that end, we focus on scalar waves and leave the potential arbitrary. In the subsequent sections, we will restrict attention to a specific system demonstrating rotational superradiance.

We assume the potential is time-independent and confined to a particular region of space, or decays rapidly outside a compact interacting region. For the sake of clarity, we momentarily focus on one-dimensional wave

propagation. Due to the time-independence of the potential, the frequency ω of the waves remains conserved. Therefore, it suffices to focus on a single frequency at a time.

Imagine a scenario akin to the one depicted in Fig. 1, where an ingoing wave packet centered around the frequency ω scatters off the potential, resulting in two outgoing wave packets, each centered at the same frequency ω . The outgoing wave packets propagate away from the potential—the reflected part towards the right and the transmitted wave packet towards the left. This scattering scenario is described by a wave Ψ such that

$$\Psi|_{t \rightarrow -\infty} = W_l^{\text{in}} \xrightarrow{\text{time}} \Psi|_{t \rightarrow \infty} = T W_l^{\text{out}} + R W_r^{\text{out}}, \quad (1)$$

where T and R denote the transmission and reflection coefficients, respectively, and the subscripts r and l indicate rightward and leftward propagation, respectively. Valuable insights into these coefficients can be obtained by examining conserved quantities of the wave equation.

To gain some intuition, we first consider a scattering process described by the standard Schrödinger equation, with $\int dx |\Psi(t, x)|^2$ being a conserved quantity. This is the familiar conservation of probability in non-relativistic quantum mechanics. This quantity is strictly positive, and equal to 1 for normalized wave packets. Equating its value at early and late times, we find $1 = |T|^2 + |R|^2$, implying that neither $|T|$ nor $|R|$ can exceed unity. In other words, amplification cannot occur in the framework of Schrödinger theory, by virtue of the conservation of probability.

Bosonic field theories behave differently. Consider a scalar field $\Phi(t, x)$ which satisfies the Klein-Gordon equation in Minkowski spacetime (the argument below readily generalizes to any globally hyperbolic curved spacetime and to other bosonic theories, such as electromagnetic fields or gravitational perturbations)

$$[\partial_t^2 - \partial_x^2 + m^2 + V(x)] \Phi(t, x) = 0, \quad (2)$$

where $V(x)$ represents an external potential, $m \geq 0$ is the mass of the field, and we are setting the speed of light to one. This constitutes a relativistic field theory, with $\Phi(t, x)$ representing the value of the Klein-Gordon field at a point in spacetime. The conserved quantity for this theory is

$$Q_{\text{KG}}(\Phi) \equiv i/\hbar \int (\Phi^* \partial_t \Phi - \partial_t \Phi^* \Phi) dx, \quad (3)$$

as can be readily checked by computing its time derivative and utilizing the Klein-Gordon equation (2) to show that it vanishes. (This quantity is commonly referred to as ‘‘symplectic norm’’). An important property of Q_{KG} is that it can take negative values. Consequently, some potentials admit scattering solutions in which the right- and left-moving scattered wave packets carry different signs of Q_{KG} . In such a scenario, the conservation of Q_{KG} yields

$$1 = ||T|^2 - |R|^2|, \quad (4)$$

which implies that $|T|$ and/or $|R|$ must be larger than unity. Therefore, there is amplification, and the scattered outgoing waves have larger amplitudes than the incident one. This is superradiance. We see that superradiance is a consequence of having modes with the same frequency but carrying opposite sign of Q_{KG} , which can be traced back to the bosonic character of the field.²

We finish this section with a simple characterization of superradiant scattering, which will be useful in the subsequent sections of this article.

Consider the scattering of two incoming wave packets depicted in Fig. 1, both narrowly centered around the frequency ω , approaching the potential from opposing directions, denoted by W_r^{in} and W_l^{in} . The scattered wave will result in a linear combination of the normalized outgoing wave packets W_r^{out} and W_l^{out} . This scattering phenomenon can be succinctly written as

$$(W_r^{\text{in}}, W_l^{\text{in}})|_{t \rightarrow \infty} = (W_r^{\text{out}}, W_l^{\text{out}}) \cdot \mathbf{B}, \quad (5)$$

where

$$\mathbf{B} = \begin{pmatrix} T & r \\ R & t \end{pmatrix}, \quad (6)$$

and $T, R, r, t \in \mathbb{C}$. The matrix \mathbf{B} describes the scattering of wave packets with central frequency ω . If the incident wave is of the form $a_1 W_r^{\text{in}} + a_2 W_l^{\text{in}}$, the scattered wave will have the form $b_1 W_r^{\text{out}} + b_2 W_l^{\text{out}}$, where $a_i, b_i \in \mathbb{C}$ are amplitudes. The incident and scattered wave amplitudes are related via

$$\begin{pmatrix} b_1 \\ b_2 \end{pmatrix} = \mathbf{B} \cdot \begin{pmatrix} a_1 \\ a_2 \end{pmatrix}. \quad (7)$$

² For fermionic fields, the conserved charge is definite positive — e.g., $Q_{\text{D}} \equiv \int dx \Psi^\dagger \Psi$ for a Dirac field — thus precluding the existence of superradiance. This positivity is directly related to the fermionic statistics and Pauli’s exclusion principle.

The main outcome of this discussion is encapsulated in the following theorem, the proof of which can be found in Appendix A.

Theorem 1: The matrix \mathbf{B} describing the scattering from IN to OUT modes off a time-independent potential corresponds to superradiant scattering if and only if it is not a unitary matrix.

III. QUANTUM DESCRIPTION OF SUPERRADIANCE

A simple way to translate the classical scattering described by Eqn. (5) to the quantum theory, is to recall that each normalized wave packet W_i , where i denotes a collective label, defines a creation and annihilation operator as follows. Consider the operator defined as

$$i/\hbar \int (W_i^* \partial_t \hat{\Phi} - \partial_t W_i^* \hat{\Phi}) dx, \quad (8)$$

where $\hat{\Phi}(t, x)$ is the bosonic field operator. We will call this operator \hat{a}_i whenever $Q_{\text{KG}}(W_i) = 1$, and $-\hat{a}_i^\dagger$ if $Q_{\text{KG}}(W_i) = -1$.

Using the canonical commutation relations for $\hat{\Phi}(t, x)$ and its conjugate momentum $\partial_t \hat{\Phi}(t, x)$, one can check that $[\hat{a}_i, \hat{a}_i^\dagger] = |Q_{\text{KG}}(W_i)| = 1$. Hence, these are creation and annihilation operators, whose associated quanta are described by the wave packet W_i . We can define in this way a pair of such operators for each of the four wave packets involved in the scattering process. The creation and annihilation operators defined for the left- and right-moving IN modes commute, and the same holds for the OUT modes. The quantum scattering for a fixed central frequency ω is thus described by the vector equation

$$\hat{\mathbf{A}}_{\text{out}} = \mathbf{S} \cdot \hat{\mathbf{A}}_{\text{in}}, \quad (9)$$

where

$$\hat{\mathbf{A}}_{\text{out}} = \begin{pmatrix} \hat{a}_r^{\text{out}} \\ \hat{a}_l^{\text{out}} \\ \hat{a}_r^{\text{out} \dagger} \\ \hat{a}_l^{\text{out} \dagger} \end{pmatrix}, \quad \hat{\mathbf{A}}_{\text{in}} = \begin{pmatrix} \hat{a}_r^{\text{in}} \\ \hat{a}_l^{\text{in}} \\ \hat{a}_r^{\text{in} \dagger} \\ \hat{a}_l^{\text{in} \dagger} \end{pmatrix}, \quad (10)$$

and \mathbf{S} is a complex 4×4 matrix. As described in some detail in Appendix B, \mathbf{S} is a symplectic matrix.

Using Eqn. (8), which establishes the relationship between creation and annihilation operators and wave packets, it is possible to derive the matrix \mathbf{S} entirely from the elements of the matrix \mathbf{B} defined above. However, caution is required when connecting these two matrices. This is due to the fact that a wave packet W_i defines either a creation or an annihilation operator depending on the sign of $Q_{\text{KG}}(W_i)$, as indicated right below Eqn. (8). Thus, we must distinguish between non-superradiant (NSR) scattering, for which the sign of Q_{KG} is the same for all wave packets involved, and superradiant (SR) scattering, where that is not the case. Taking

this into consideration, the matrix \mathbf{S} takes the form, respectively

$$\mathbf{S}_{\text{SR}} = \begin{pmatrix} T & 0 & 0 & r \\ 0 & t^* & R^* & 0 \\ 0 & r^* & T^* & 0 \\ R & 0 & 0 & t \end{pmatrix}, \quad \mathbf{S}_{\text{NSR}} = \begin{pmatrix} T & r & 0 & 0 \\ R & t & 0 & 0 \\ 0 & 0 & T^* & r^* \\ 0 & 0 & R^* & t^* \end{pmatrix} \quad (11)$$

where the coefficients T, R, t and r are the elements of \mathbf{B} as defined in the previous section. Upon a mere inspection of these matrices, it becomes evident that superradiant scattering mixes creation and annihilation operators. This mirrors the classical scattering process, which mixes modes with different signs of $Q_{\text{KG}}(W_i)$. Conversely, this mixing does not occur in the case of non-superradiant scattering.

Using the constraints satisfied by the coefficients T, R, t and r for superradiant and non-superradiant scattering (written in Appendix A) it is easy to see that \mathbf{S}_{NSR} is a unitary matrix while \mathbf{S}_{SR} is not. We find, therefore, an application of Theorem 1 to the quantum theory: the transformations between creation and annihilation operators (9) describes superradiant scattering if and only if \mathbf{S} is not a unitary matrix.

From a physical perspective, the matrices \mathbf{S}_{NSR} and \mathbf{S}_{SR} describe very different transformations. The unitary nature of \mathbf{S}_{NSR} has physical implications: it preserves the vacuum state and also preserves the total number of quanta $\hat{N}_r^{\text{in}} + \hat{N}_l^{\text{in}}$, thus conserving energy. \mathbf{S}_{NSR} functions as a beam splitter. In contrast, \mathbf{S}_{SR} does *not* preserve either the vacuum state or the total number of particles. It does, however, leave the number difference, $\hat{N}_r^{\text{in}} - \hat{N}_l^{\text{in}}$, unchanged, implying the creation of excitations in pairs. \mathbf{S}_{SR} is a two-mode squeezer, which converts the vacuum state into a two-mode squeezed vacuum.

While it is well-known that superradiant scattering amplifies incoming field excitations, recognizing that superradiance can be described as a two-mode squeezing process reveals that wave amplification is tied to the generation of entanglement. Hence, entanglement is expected to be generated at the output both for classical and quantum input states. This is a fundamental aspect of this quantum phenomenon which highlights its entanglement-generating capabilities.

A. Generation of entanglement

In the remainder of this section, we quantify the entanglement generated by superradiant scattering for three representative initial states, namely vacuum, a coherent state, and a single-mode squeezed state.

We consider a coherent state centered at $\langle \hat{a}_r \rangle = \gamma_r$ and $\langle \hat{a}_l \rangle = \gamma_l$, with $\gamma_r, \gamma_l \in \mathbb{C}$.

A single-mode squeezed state is obtained by acting with a squeezing operator on one of the two IN modes,

for instance, the left-mover W_l^{in}

$$|z_l, \phi_l\rangle_{\text{sqs}} = e^{\xi_l \hat{a}_l^\dagger - \xi_l^* \hat{a}_l} |0\rangle, \quad (12)$$

where $\xi_l = e^{i\phi_l} z_l$, and ϕ_l, z_l are real numbers representing the squeezing angle and intensity, respectively. These three states are pure and separable, meaning there is no initial entanglement between the two IN modes.

We evolve these Gaussian states using \mathbf{S}_{SR} , and quantify entanglement between the two OUT modes on either side of the potential barrier via the entanglement entropy $S_{\text{ent}}(\omega)$. For this calculation, we use the tools spelled out in Appendix B.³

First, we calculate the flux (number of quanta per unit time and unit bandwidth) in each of the outgoing modes in terms of the elements of \mathbf{S}_{SR} . For the two-mode vacuum, we find

$$\langle \hat{N}_r^{\text{out}} \rangle = \langle \hat{N}_l^{\text{out}} \rangle = |R|^2. \quad (13)$$

For the two-mode coherent state, we obtain

$$\langle \hat{N}_r^{\text{out}} \rangle = |\gamma_r|^2 + |R|^2 + |R|^2 (|\gamma_r|^2 + |\gamma_l|^2) + 2\text{Re}[r^* T \gamma_r \gamma_l], \quad (14)$$

$$\langle \hat{N}_l^{\text{out}} \rangle = |\gamma_l|^2 + |R|^2 + |R|^2 (|\gamma_l|^2 + |\gamma_r|^2) + 2\text{Re}[t^* R \gamma_l \gamma_r]. \quad (15)$$

Finally, for the one-mode squeezed state

$$\langle \hat{N}_r^{\text{out}} \rangle = |R|^2 + |R|^2 \sinh^2 z_l, \quad (16)$$

$$\langle \hat{N}_l^{\text{out}} \rangle = \sinh^2 z_l + |R|^2 + |R|^2 \sinh^2 z_l. \quad (17)$$

In Eqs. (14) and (15), the first term corresponds to the finite number of quanta already present at the input, while the second term, equal to $|R|^2$, represents the amplification of vacuum fluctuations (13). The third and fourth terms represent stimulated emission (amplification) due to superradiance. Likewise, in Eqs. (16) and (17), $|R|^2$ corresponds to amplification of vacuum fluctuations while $|R|^2 \sinh^2 z_l$ manifests amplification of the number of quanta in the mode W_l^{in} present in the initial state.

Importantly, not all created pairs at the output are entangled: superradiant scattering does not yield the same emission statistics for all input states. Fig. 2 shows the entanglement entropy of the output $S_{\text{ent}}(\omega)$ (i.e., the von Neumann entropy of either of the two output modes) as a function of $|R|$ for the three input states (and two values of initial squeezing in W_l^{in}). On the one hand, we see that $S_{\text{ent}}(\omega)$ is identical for vacuum and coherent input states. This implies that, even though the amplitude

³ In section VI, we extend the analysis presented here by considering thermal noise at the input as well as losses and detector inefficiencies.

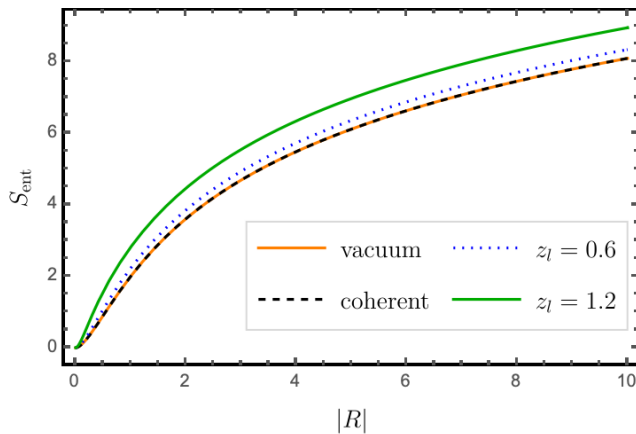


FIG. 2. Entanglement entropy, $S_{\text{ent}}(\omega)$, of the OUT modes as a function of the absolute value of the scattering coefficient R . We plot the result for different inputs: vacuum, an arbitrary coherent state (this plot is insensitive to γ_r and γ_l), and states where the left IN mode is in vacuum but the right one is squeezed with squeezing intensity z_l (the plot is insensitive to the squeezing angle ϕ_l). To produce the plot, we have assumed, without loss of generality, that $Q(W_r^{\text{in}}) = Q(W_r^{\text{out}})$, so that $|T|^2 \geq 1$.

of the coherent state gets enhanced after the scattering, entanglement at the output is due to the amplification of vacuum fluctuations only. On the other hand, the amplification of single-mode squeezed states is different: $S_{\text{ent}}(\omega)$ is higher than for the other two input states for all values of z_l . So, in this case, entanglement at the output does not come exclusively from vacuum amplification—single-mode squeezing at the input enhances entanglement at the output. Hence, we observe that superradiant scattering not only amplifies incoming radiation, but also its quantum properties.⁴

IV. STABLE ERGOREGIONS IN POLARITON FLUIDS

Because of the spontaneous amplification of vacuum fluctuations by rotational superradiance, ergoregions are intrinsically dynamically unstable [20–22]. In this section, we propose that dissipative dynamics can quench this instability. We evidence this numerically by engineering a stable ergosurface in a driven-dissipative fluid of light realized with microcavity exciton-polaritons (polaritons). We also present experimental data reproducing the numerical configuration.

Polaritons are half-light half-matter bosonic quasiparticles resulting from the strong coupling of photons in a semiconductor cavity with an excitonic tran-

⁴ A similar effect occurs in pair production from causal horizons, i.e., Hawking radiation.

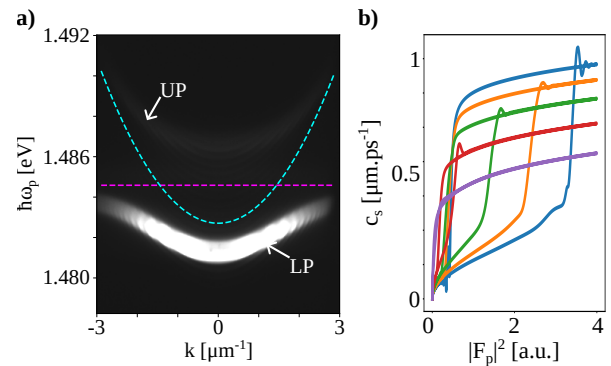


FIG. 3. Microcavity polaritons. **a)** Dispersion of the light coming from the cavity (experimental measurement). Dashed turquoise: cavity photons; dashed purple: excitons; UP: upper polaritons; LP: lower polaritons. Exciton-photon energy difference -1.88 meV. **b)** Optical bistability of the LP for a homogeneous fluid with $\delta_{k_p=0} = 0.618$ meV incident on the cavity at different k_p (numerical calculation): blue, $k_p = 0$ μm^{-1} ; orange, $k_p = 0.2$ μm^{-1} ; green, $k_p = 0.3$ μm^{-1} ; red, $k_p = 0.4$ μm^{-1} ; purple, $k_p = 0.5$ μm^{-1} .

sition [23]. Their dynamics in the cavity plane are intrinsically driven-dissipative, with steady-states reached only through constant pumping with a continuous wave laser. All properties of the quantum fluid in the cavity are controlled by the pump laser and measured via photons exiting the cavity.

A. Microcavity polaritons

We consider a laser field inside a semiconductor microcavity made of quantum wells sandwiched between two Bragg mirrors. Under the resonance-induced quantization of the photon wavevector perpendicular to the cavity, photons acquire an effective mass 5 orders of magnitude lower than the mass of the electron.

Cavity photons excite electric dipoles (bound electron-hole states) called excitons, which are massive self-interacting excitations. The strong coupling of photons and excitons generates two new eigenstates of the system: two polariton branches with different dispersive properties, the upper and the lower polaritons (see Fig. 3). In practice, only the lower polaritons LP are excited and measured in the experiment.⁵

Polaritons inherit the properties of cavity photons and excitons, and thus behave collectively as an ensemble of self-interacting massive particles—a quantum fluid of light [23–28].

⁵ Since the Rabi energy $\hbar\Omega_R$, controlling the gap between the upper and lower polariton branches, is much larger than the characteristic energies of the system, in particular the interaction energy $\hbar g n$, the fluid contains only lower polaritons, so its wavefunction may be truncated to that of the lower polaritons $\psi(\mathbf{r}, t) = \psi_{LP}(\mathbf{r}, t)$.

Because of the decay of excitons and cavity photons, polaritons are unstable and decay with a rate γ , yielding photons exiting the cavity at the same rate. These photons carry all the information of the phase and intensity of the intra-cavity polariton field, allowing us to measure the quantum properties of the fluid with optical detectors.

The mean field $\psi(\mathbf{r}, t)$ of the polariton fluid is governed by the driven-dissipative Gross-Pitaevski equation [23]

$$i\hbar \frac{\partial \psi}{\partial t} = \left(\hbar\omega_{LP} - \frac{\hbar^2 \nabla^2}{2m_{LP}} + \hbar g |\psi|^2 - i\hbar \frac{\gamma}{2} \right) \psi + i\hbar \mathcal{F}(\mathbf{r}, t), \quad (18)$$

where ω_{LP} is the frequency of polaritons at wavevector $\mathbf{k} = 0$, $-\hbar^2 \nabla^2 / 2m_{LP}$ their kinetic energy in the cavity plane, m_{LP} their effective mass, $\hbar g$ the strength of repulsive polariton self-interactions and $\mathcal{F}(\mathbf{r}, t) = F_p(\mathbf{r})e^{i(\phi_p(\mathbf{r}) - \omega_p t)}$ represents the electromagnetic field of the laser pump.

Eqn. (18) can be rewritten in terms of the density n and phase ϕ_{LP} of the fluid by $\psi = \sqrt{n}e^{i\phi_{LP}}$, which leads to its hydrodynamical—or Madelung—representation. The resulting equations are the continuity and Euler equations for a fluid with density n and velocity $\mathbf{v}(\mathbf{r}) = \hbar \nabla \phi_{LP} / m_{LP}$.

If the laser frequency ω_p is near resonance with the lower polariton branch, the steady state of the polariton fluid is controlled by the pump. Concretely, its phase is inherited from the pump, $\psi(\mathbf{r}, t) = \sqrt{n(\mathbf{r})}e^{i(\phi_p(\mathbf{r}) - \omega_p t)}$, and its density is related to the intensity of the pump and the detuning according to Eqn. (18). In particular, for a homogeneous steady-state configuration excited by a plane wave at k_p , in the rest frame of the fluid we find the equation of state

$$n \left[\left(\frac{\gamma}{2} \right)^2 + (gn - \delta)^2 \right] = |F_p|^2, \quad (19)$$

with $\delta = \omega - \omega_{LP} - \hbar k_p^2 / 2m_{LP}$ the effective detuning. The number of solutions to this equation crucially depends on the value of this detuning: for $\delta > \sqrt{3}\gamma/2$, there can be either three or one solution depending on the pump intensity. This leads to a hysteresis loop, shown in Fig. 3 b), where the fluid can either be in a high or low density regime for some values of the pump intensity, known as optical bistability [29].

Collective excitations of the polariton fluid are studied by linearizing Eqn. (18) via $\psi(\mathbf{r}, t) = (\psi^0 + \delta\psi)e^{i(\phi_p(\mathbf{r}) - \omega_p t)}$. Their spectrum in a spatially homogeneous region is given by the Bogoliubov dispersion relation, which is a quadratic form admitting two $\{k, \omega\}$ solutions at positive laboratory-frame frequencies ω [23, 30]. While these roots can be complex, when they are real there are two frequency solutions at each wavenumber [23, 30]: positive (negative) rest-frame frequency modes have a positive (negative) norm (8) [31].

The inhomogeneous mean field $\psi^0 e^{i(\phi_p(\mathbf{r}) - \omega_p t)}$ sets the kinematics of the collective excitations $\delta\psi$ (which effec-

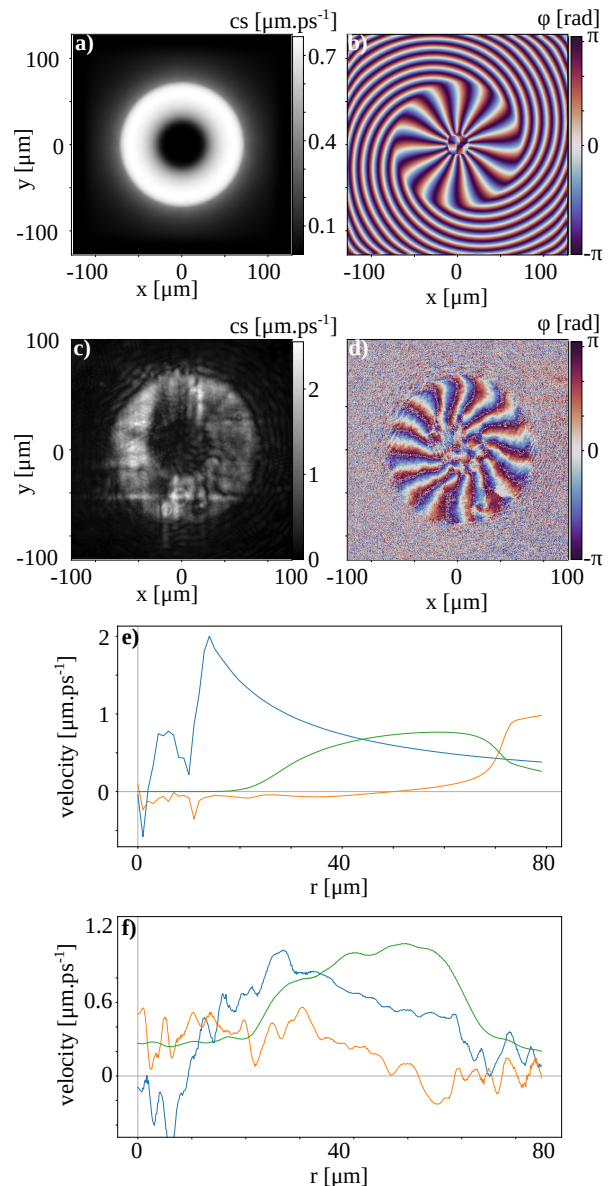


FIG. 4. Vortex flow in a polariton fluid with $D = 0$ and $C = 15$. **a**), **b**) and **e**) numerical simulation of Eqn. (18). **c**), **d**) and **f**) experimental data (azimuthal average). **a**), **c**) speed of sound c_s ; **b**), **d**) phase ϕ_{LP} ; **e**), **f**) Velocities versus a radius. Blue: v_θ ; orange: v_r ; green: c_s .

tively behaves as a Klein-Gordon field) [32, 33]. Depending on the fluid velocity profile $\mathbf{v}(\mathbf{r})$ and the speed of sound $c_s(\mathbf{r}) = \sqrt{\hbar g n(\mathbf{r}) / m}$ in the inhomogeneous flow, we can find configurations in which $\delta\psi$ experiences a scattering process as the one described in Eqn (11). Specifically, there exist positive laboratory-frame frequencies at which there are two positive-norm ($Q_{KG} > 0$) modes in some region of space and two negative-norm ($Q_{KG} < 0$) modes in some other region of space. In addition, in each spatial region, the two modes always have opposite sign of group velocity. This configuration corresponds to superadiant scattering.

B. Numerics and experiment

Control of the fluid phase and density via the properties of the pump laser allows us to engineer polariton vortices by shaping the pump field into an optical vortex with $\phi_p(r, \theta) = D(r) + C\theta$, with (r, θ) being polar coordinates in the plane and where we have imposed rotational symmetry. The function $D(r)$ and the parameter C control the flow velocity, whose target velocity profile is

$$\mathbf{v}(r) = \frac{\hbar}{m_{LP}} \left(\frac{dD}{dr} \hat{\mathbf{r}} + \frac{C}{r} \hat{\boldsymbol{\theta}} \right), \quad (20)$$

where hats denote unit vectors. In the experiment, we create a vortex with $D = 0$, $C = 15$.

Our semiconductor microcavity is made of two planar GaAs/AlGaAs Bragg mirrors, separated from each other by a 2λ -thick GaAs substrate forming a high finesse ($\mathcal{F} = 3000$) optical cavity. Three InGaAs quantum wells are embedded at the antinodes of the cavity field. The sample is cooled to approximately $6K$, and we measure a Rabi energy $\hbar\Omega_R = 5.07$ meV, a polariton mass of 5.7×10^{-35} kg as well as a polariton linewidth $\hbar\gamma = 0.08$ meV. A small wedge between the cavity mirrors leads to a spatial energy gradient of the bottom of the lower polariton branch of about $0.7 \mu\text{eV} \mu\text{m}^{-1}$ along the cavity axis.

Firstly, we numerically simulate the polariton dynamics described by Eqn. (18). Fig. 4 a), b) and e) shows the numerical data.

The fluid density (we show $c_s(\mathbf{r})$ as a proxy to n) assumes the annular shape characteristic of polariton vortices. The density is high enough to enable the nonlinear regime of interactions over $r \in [25, 70] \mu\text{m}$.

The phase $\phi_p(r, \theta)$, shown in Fig. 4 b), features 15 jumps from 0 to 2π , indicating finite circulation of the phase along any given radius. The negligible curvature of phase jumps along r in the high-density region manifests the near zero radial velocity v_r of the fluid, as confirmed by the corresponding orange line nearing zero in Fig. 4 f). This implies that, in this configuration, $\mathbf{v} = v_\theta \hat{\boldsymbol{\theta}}$. In our driven-dissipative fluid, the frequency detuning δ contributes to a gap between positive- and negative-norm modes (see also Appendix C for a discussion about the gap). Because of this gap, negative-norm modes oscillate at positive laboratory-frame frequencies for $r \leq r_e = 40 \mu\text{m}$, inside $r|_{v|=c_s} = 43 \mu\text{m}$ where the azimuthal and sound velocities cross. r_e defines the ergosurface that bounds the ergoregion in our numerical configuration.

The numerical data of Fig. 4 corresponds to the steady-state (19), so the configuration is evidently dynamically stable. Note that the steady-state is reached despite the presence of an ergosurface. In numerical calculations, we have studied the exact solutions to the field equations in the hydrodynamic regime and confirmed that rotational superradiance can occur in this configuration (for additional details, see discussion below Eqns. (29) and Appendix C). As a result, negative-norm modes in the

ergoregion will have a finite amplitude even in the presence of vacuum fluctuations only (omitting e.g. thermal fluctuations). However, these excitations propagate with a velocity comparable to $c_s \leq 0.7 \mu\text{m ps}^{-1}$. Given that the value of γ corresponds to a lifetime of ≈ 8 ps, the mean free path of these excitations is $\approx 6 \mu\text{m}$. In other words, for the same reason that the polariton density drops towards short radii, negative-norm excitations will not be able to propagate across the vortex and reach the ergosurface on the other side. The finite lifetime of polaritons quenches the characteristic instability of horizonless ergoregions.⁶

Next, we present the experimental creation of an irrotational vortex. A continuous-wave Ti:Sapphire pump laser (linewidth < 1 MHz) illuminates the cavity with a beam waist of $\approx 100 \mu\text{m}$. The phase and intensity profiles of the pump are controlled with a spatial light modulator (SLM) in order to create an optical vortex. Its frequency is slightly blue detuned from the polariton resonance ($\delta_{k_p=0} = 0.618$ meV $> \sqrt{3}\gamma/2$) so as to operate in the bistable regime.

Light transmitted by the cavity is interfered with a reference beam (picked up from the pump before the SLM) on a beam-splitter and the resulting interference pattern is imaged by a camera, allowing to measure the phase and intensity of the intra-cavity field with off-axis interferometry.

Fig. 4 c), d) and f) shows the experimental data. The density is high enough to enable the nonlinear regime of interactions over $r \in [25, 60] \mu\text{m}$.⁷ The radial velocity v_r (orange curve in Fig. 4 f)) is finite but small with respect to v_θ for $r > 40 \mu\text{m}$. v_r grows towards the center and crosses c_s (green curve) at $r = 20 \mu\text{m}$. However, self-interactions are negligible there, so there is no horizon in this configuration. The blue line in Fig. 4 f) shows the growth of v_θ at small radii, with a velocity crossing at $r = 36 \mu\text{m}$. The experimental data qualitatively reproduces the numerical configuration.

To conclude, in this section we have numerically shown that stable, horizonless ergoregions can be created in polariton fluids, while experimental data indicates that such experiments can indeed be carried out.

V. ROTATIONAL SUPERRADIANCE IN A QUANTUM FLUID OF LIGHT

In this section we describe the conditions under which collective excitations in the quantum fluid undergo su-

⁶ In our configuration, the phase is set by the resonant pump, so the stabilization dynamics are different from configurations in which the phase is left free, eg in the formation of multiply charged vortices upon Bose-Einstein condensation [34].

⁷ The large fluctuations in the radial and azimuthal velocities at short and large radii stem from the limited visibility of the interference fringes due to the low intensity of the intra-cavity field there.

perradiant scattering at the ergosurface.

In the hydrodynamic limit, the scalar field of collective excitations $\delta\psi$ follows the equation

$$\left[(\partial_t + \mathbf{v} \cdot \nabla)^2 - c_s^2 \nabla^2 + c_s^2 \left(\nabla \cdot \frac{\mathbf{v}}{c_s^2} \right) (\partial_t + \mathbf{v} \cdot \nabla) \right] \delta\psi(t, r, \theta) = 0. \quad (21)$$

In this section, we take c_s constant and use a velocity profile $\mathbf{v}(r) = v_\theta(r)\hat{\theta}$. Eqn. (21) simplifies to

$$\left[(\partial_t + \mathbf{v} \cdot \nabla)^2 - c_s^2 \Delta \right] \delta\psi(t, r, \theta) = 0. \quad (22)$$

The form of this equation suggests defining the time coordinate \tilde{t} associated with a frame co-rotating with the fluid, such that $\partial_{\tilde{t}} = \partial_t + \mathbf{v} \cdot \nabla = \partial_t + \frac{v_\theta}{r} \partial_\theta$.

Solutions to (22) are combinations of cylindrical waves of the form

$$\delta\psi_{\omega, \ell}(t, r, \theta) = e^{-i\omega t} e^{i\ell\theta} \varphi_{\omega\ell}(r), \quad (23)$$

with $\varphi_{\omega\ell}(r)$ a solution of the radial differential equation

$$\left[\frac{1}{r} \frac{d}{dr} \left(r \frac{d}{dr} \right) + V_{\omega\ell}(r) \right] \varphi_{\omega\ell}(r) = 0, \quad (24)$$

where

$$V_{\omega\ell}(r) = \frac{1}{c_s^2} \left(\omega - \frac{v_\theta(r)\ell}{r} \right)^2 - \frac{\ell^2}{r^2}. \quad (25)$$

The symmetries of the problem ensure the conservation of both ω and ℓ . Therefore, modes characterized by different ω or ℓ values remain decoupled throughout their evolution, and it suffices to describe each of them individually. We drop these labels from now on to simplify the notation.

From Eqn. (24), we see that wave scattering in this configuration reduces to a one-dimensional problem in the radial direction, described by the effective potential $V_{\omega\ell}(r)$:

$$(W_r^{\text{in}}, W_l^{\text{in}}) \xrightarrow{\text{time}} (W_r^{\text{out}}, W_l^{\text{out}}) \cdot \mathbf{B}. \quad (26)$$

with “ r ” and “ l ” corresponding to propagation in the radial direction, denoting local out- and inward propagating modes respectively.

We model the velocity profile v_θ/c_s across the ergosurface with

$$v_\theta(r) = \frac{\alpha_1}{2} [1 + \tanh \alpha_2(\alpha_3 - r)], \quad (27)$$

which is parameterized by three constants, α_i , $i = 1, 2, 3$. As shown in Fig. 5, the variation from $v_\theta = \alpha_1$ for $r \ll \alpha_3$ to $v_\theta \rightarrow 0$ as $r \gg \alpha_3$ is monotonous, while α_2 governs the sharpness of the transition between the two asymptotic values of v_θ . Choosing α_1 exceeding c_s ensures the

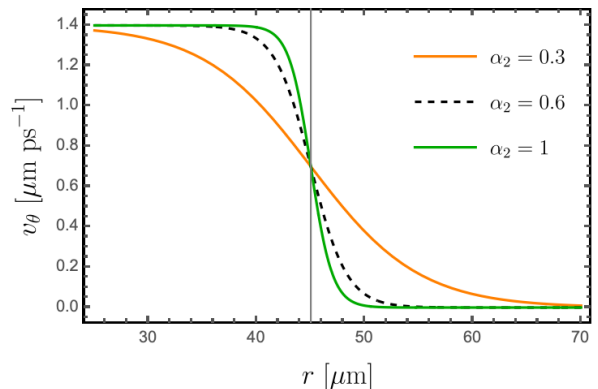


FIG. 5. Velocity profile in (27) with $\alpha_1 = 2c_s$, with $c_s = 0.7\mu\text{m ps}^{-1}$, and $\alpha_3 = 45\mu\text{m}$. The grey vertical line signals the position of the ergosurface.

existence of an ergoregion at small radii, with its boundary situated at r_e , defined by $v_\theta(r_e) = c_s$. We choose $\alpha_1 = 2c_s$ with $c_s = 0.7\mu\text{m ps}^{-1}$ and $\alpha_3 = 45\mu\text{m}$, as suggested by the values in Fig. 4, and $\alpha_2 = 0.3\mu\text{m}^{-1}$. This velocity profile is relevant only for radii greater than r_{min} , below which the fluid density is insufficient to support the propagation of acoustic waves.

The conserved quantity (2) associated with the equation of motion (22) reads

$$Q_{\text{KG}}(\phi) = i/\hbar \int_0^\infty dr \int_0^{2\pi} d\theta \frac{r}{c_s^2} [\phi^* \partial_{\tilde{t}} \phi - \partial_{\tilde{t}} \phi^* \phi], \quad (28)$$

implying that modes with $\tilde{\omega} > 0$ ($\tilde{\omega} < 0$), as defined by the time derivative $\partial_{\tilde{t}}$, have positive (negative) norm Q_{KG} .

Given that v_θ diminishes for large radii, in this asymptotic region ($r \gg r_e$) we have $\partial_{\tilde{t}} = \partial_t$, and $\tilde{\omega} = \omega$. Consequently, the sign of Q_{KG} for wave packets initially localized at large radii is determined by the sign of ω . This scenario applies to the wave packets W_l^{in} and W_r^{out} in our scattering analysis, since they are localized at large radii at early and late times, respectively. Since Q_{KG} remains conserved throughout their evolution, these wave packets bear positive Q_{KG} at all times when $\omega > 0$.

Conversely, for wave packets localized in the vicinity of $r \approx r_{\text{min}}$, $\tilde{\omega} = \omega - \frac{v_\theta(r_{\text{min}})}{r_{\text{min}}} \ell$. Consequently, they possess negative Q_{KG} values when $\left(\omega - \frac{v_\theta(r_{\text{min}})}{r_{\text{min}}} \ell \right) < 0$. This applies to the modes W_r^{in} and W_l^{out} , which are localized near r_{min} at early and late times, respectively.

In brief, whenever ω and $\left(\omega - \frac{v_\theta(r_{\text{min}})}{r_{\text{min}}} \ell \right)$ have different signs, we expect superradiant scattering to occur at the ergosurface.

Next, we proceed to solve the scattering process between the IN and OUT wave packets. Exact solutions to the radial Eqn. (24) exist when the velocity v_θ remains constant along the radial direction. In such a scenario, a

basis of solutions is provided by Whittaker functions

$$\begin{aligned} & \frac{1}{\sqrt{r}} \text{WhittakerM} \left(i\ell \frac{v_\theta}{c}, \ell \sqrt{1 - \frac{v_\theta^2}{c^2}}, i \frac{2\omega}{c} r \right), \\ & \frac{1}{\sqrt{r}} \text{WhittakerW} \left(i\ell \frac{v_\theta}{c}, \ell \sqrt{1 - \frac{v_\theta^2}{c^2}}, i \frac{2\omega}{c} r \right), \end{aligned} \quad (29)$$

which reduce to Bessel functions in the homogeneous limit $v_\theta \rightarrow 0$. (In the definition of these functions, we adhere to the same conventions as those used in the software `Mathematica`.)

At a given radius r , these solutions can have either locally oscillatory or evanescent behavior, depending on the values of $\omega - \frac{v_\theta(r)}{r} \ell$. The behavior of a mode (ω, ℓ) is determined by the WKB dispersion relation, which has a position-dependent gap equal to $2c_s \ell / r$ (see Appendix C). To a good approximation, if the frequency of a mode falls within this gap, wave packets constructed from them are evanescent (they do not describe propagating modes). Evanescent modes are not part of the IN and OUT bases. As for propagating modes, negative-norm modes at inner radii have frequency $\omega - \frac{v_\theta(r_{\min})}{r_{\min}} \ell < -\frac{c_s}{r_{\min}} \ell$, while positive-norm modes at $r_{\max} \gg \alpha_3$ have frequency $\omega - \frac{v_\theta(r_{\max})}{r_{\max}} \ell < -\frac{c_s}{r_{\max}} \ell$. In our system, the laboratory-frame frequency window of superradiant scattering is thus $6.54 \ell < \hbar\omega < 18.31 \ell$ (in μeV).

The velocity profile (27) remains independent of r , except in the vicinity of $r = \alpha_3$. Consequently, we can employ exact solutions (29) to define the IN and OUT modes within the asymptotic regions $r \sim r_{\min}$ and $r \gg \alpha_3$, respectively. Purely incoming or outgoing waves are represented by specific linear combinations of these exact solutions, and in each of the asymptotic regions take the form

$$\begin{aligned} & \exp \left\{ \pm i \left(\frac{\omega r}{c} - \frac{\ell v_\theta(r_{\min})}{c_s} \log \frac{r}{r_{\min}} \right) \right\} \quad \text{for } r \rightarrow r_{\min}, \\ & \exp \left\{ \pm i \left(\frac{\omega r}{c} - \frac{\ell v_\theta(r_{\max})}{c_s} \log \frac{r}{r_{\max}} \right) \right\} \quad \text{for } r \rightarrow r_{\max}, \end{aligned} \quad (30)$$

We construct the wave packets W_r^{in} , W_r^{out} , W_l^{in} , and W_l^{out} , each associated with an azimuthal number ℓ and narrowly centered at frequency ω , from these radial functions multiplied by $e^{-i\omega t} e^{i\ell\theta}$. We then proceed to numerically solve the evolution of the IN wave packets with the velocity profile (27) (see Appendix D for details).

Numerical calculations are needed because of the absence of closed analytical solutions for the radial differential equations corresponding to the velocity profile (27). We numerically solve the scattering problem across a parameter space grid encompassing (ω, ℓ) . As explained above, we consider frequencies in the range $6.54 \ell < \omega < 18.31 \ell$ in μeV for each ℓ , which remain well within the hydrodynamical regime, and for which the modes scatter superradiantly. For illustrative purposes, we consider values of ℓ within the range (1, 4).

The outcomes of these calculations are the elements of the scattering matrix

$$\mathbf{B}_{\omega\ell} = \begin{pmatrix} T_{\omega\ell} & r_{\omega\ell} \\ R_{\omega\ell} & t_{\omega\ell} \end{pmatrix}. \quad (31)$$

The resulting values of these coefficients corresponding to the selected values of ω and ℓ are displayed in the tables of Table I in Appendix D. All figures in the subsequent section are based on these calculated values. As an illustrative example, we present here the scattering coefficients corresponding to $\omega = 17.00 \mu\text{eV}$ and $\ell = 1$:

$$\mathbf{B}_{\omega\ell} = \begin{pmatrix} 1.377 + 0.990i & 1.296 + 0.444i \\ -1.296 - 0.444i & -1.695 - 0.069i \end{pmatrix}. \quad (32)$$

This is *not* a unitary matrix, which confirms, in accordance with Theorem 1 in Section II, that the scattering process exhibits superradiance.⁸ Furthermore, one can check that these numerically obtained coefficients satisfy the constraints in (A6).

VI. SUPERRADIANT PRODUCTION OF ENTANGLEMENT

The calculations in the previous section yield the scattering coefficients $T_{\omega\ell}$, $R_{\omega\ell}$, $t_{\omega\ell}$, and $r_{\omega\ell}$ for the relevant range of ω and ℓ —the superradiant modes within the hydrodynamical approximation. By substituting these coefficients into expression (11), we derive the matrix $\mathbf{S}_{SR}^{\omega\ell}$, which describes the quantum scattering process for each mode (ω, ℓ) . This matrix provides all the information necessary to analyze the scattering, once the initial quantum state is specified. The primary objective of this section is to compute the entanglement between the two OUT modes following the scattering, considering a family of physically interesting initial states.

The content of this section shares certain similarities with the calculations performed in section III, with a significant distinction being that, while the description in section III was generically applicable to any superradiant process, we focus here on the specific rotating quantum fluid examined in the preceding sections. We also make use of the velocity profile depicted in Fig. 5.

For the initial state of acoustic perturbations, we first consider a thermal state at temperature T_{env} , in order to incorporate thermal noise, a common element in real experiments. It will become evident that the temperature T_{env} influences the entanglement generated during the scattering in an important manner.

⁸ As an additional verification, we have confirmed that, if we extend our calculations to higher frequencies, the numerically obtained scattering matrix indeed becomes unitary outside of the superradiant regime, serving as a test of our theoretical framework.

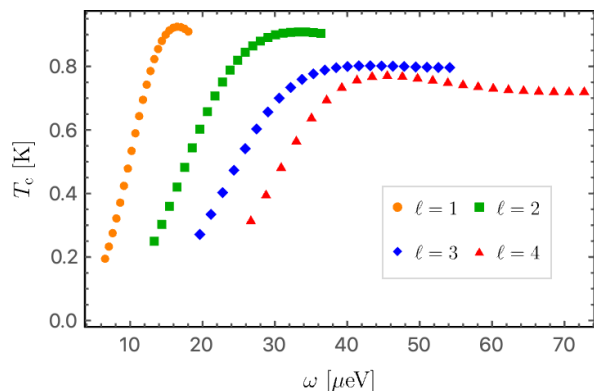


FIG. 6. Critical temperature, T_c , above which entanglement at the output vanishes, assuming vacuum input for all modes. Only frequencies describing propagating superradiant modes are shown.

However, given that thermal states are mixed quantum states, entanglement entropy is no longer applicable to quantify entanglement, as entropy measures entanglement only when the total state is pure. An easily computable entanglement metric suitable for both mixed and pure states is the Logarithmic Negativity (LN) [35–37]. It is defined as

$$\text{LN}(\hat{\rho}) = \log_2 \|\hat{\rho}^{\text{T}A}\|_1, \quad (33)$$

where $\hat{\rho}$ represents the density matrix of the system, $\hat{\rho}^{\text{T}A}$ is its partial transpose with respect to one of the two subsystems, which we denote as A , and $\|\cdot\|_1$ is the trace norm. A non-zero value of LN indicates a violation of the Positivity of Partial Transpose criterion for quantum states [35]. For Gaussian states, and when one subsystem contains a single mode, regardless of the size of the other subsystem, LN is non-zero if and only if the state is entangled. Furthermore, LN is a faithful quantifier of entanglement, meaning that a higher LN value corresponds to a greater degree of entanglement. In our calculations, we will restrict to Gaussian states, which encompass the vacuum, coherent, squeezed, and thermal states. This family is sufficiently comprehensive to describe many interesting states in our setup. Additionally, evolving Gaussian states through a scattering process described by $\mathcal{S}_{SR}^{\omega\ell}$ or, more generally, by any Hamiltonian quadratic in the fields, can be efficiently accomplished using the Gaussian formalism (see, [38, 39] for reviews). While not needed for an understanding of the results in this section, we have succinctly compiled the necessary tools to reproduce our calculations in Appendix B.

To facilitate comparison, we first show in Figs. 7 our results for vacuum input. As this is a pure state, entanglement can be quantified through entanglement entropy. This plot manifestly shows that pair-creation at the ergoregion involves generation of quantum entanglement.

Conversely, Fig. 8 shows the LN for a thermal input with various environmental temperatures, and for the $\ell = 1$ modes (the result for other values of ℓ is quali-

tatively similar). This figure reveals that the presence of thermal quanta in the initial state hinders the generation of entanglement. This outcome aligns with the intuitive notion that thermal fluctuations act as an effective source of noise, contributing to the decoherence of the system and consequently reducing entanglement. In fact, for each mode (ω, ℓ) , there exists a threshold temperature beyond which the two out modes are not entangled. This “critical” temperature is given by

$$T_c(\omega, \ell) = \frac{\hbar\omega/k_B}{\ln \left[1 + \left(|R_{\omega\ell}| (|R_{\omega\ell}| + \sqrt{1 + |R_{\omega\ell}|^2}) \right)^{-1} \right]},$$

where $R_{\omega\ell}$ are the reflection coefficients, which we have obtained numerically, and k_B is Boltzman’s constant. Fig. 6 shows $T_c(\omega, \ell)$ for $\ell = 1, 2, 3$ and 4, and for the relevant range of frequencies. This threshold temperature is important for experimental efforts seeking to detect entanglement. The range of temperatures at which entanglement exists is within current experimental capabilities with state-of-the-art cryostats.

All the findings discussed thus far remain unaffected if we replace the initial state with a coherent state. This holds true whether we consider a pure coherent state at zero temperature or add thermal noise to it. The rationale behind this is that a coherent state differs from the vacuum solely through a displacement of the mean value of the field operator, which entanglement remains insensitive to. Consequently, while the number of quanta in each of the OUT modes is amplified when the input is a coherent state (according to formulas (14) and (15)), entanglement remains unaffected.

Next, we discuss superradiant amplification of entanglement. As described in Section III, entanglement in the final state can be amplified by illuminating the ergoregion with a thermal-single-mode squeezed state. This state stems from the application of a single-mode squeezer operator, $e^{\xi_l \hat{a}_l^\dagger - \xi_l^* \hat{a}_l}$, to a thermal state ($\xi_l = z_l e^{i\phi_z}$). In keeping with Section III, we focus on squeezing the left-moving IN mode. It is worth noting that this initial state does not contain any entanglement between the two IN modes. However, initial squeezing represents a quantum resource [40, 41], and the ergoregion has the capability to transform it into entanglement. Consequently, the resulting OUT state exhibits a higher degree of entanglement compared to what would have been achieved with thermal or coherent-thermal inputs at the same temperature. This amplification serves to counterbalance the detrimental effects of thermal noise.

These effects are shown in the right panel of Fig. 7 and in Fig. 9. In particular, the latter figure illustrates how initial squeezing can maintain the OUT state entangled, even for temperatures exceeding the threshold value that would render the state separable in the absence of initial squeezing.

To finish, we discuss the impact of losses, or detector inefficiencies, and their impact on the entanglement in the OUT state. A suitable estimation of these effects

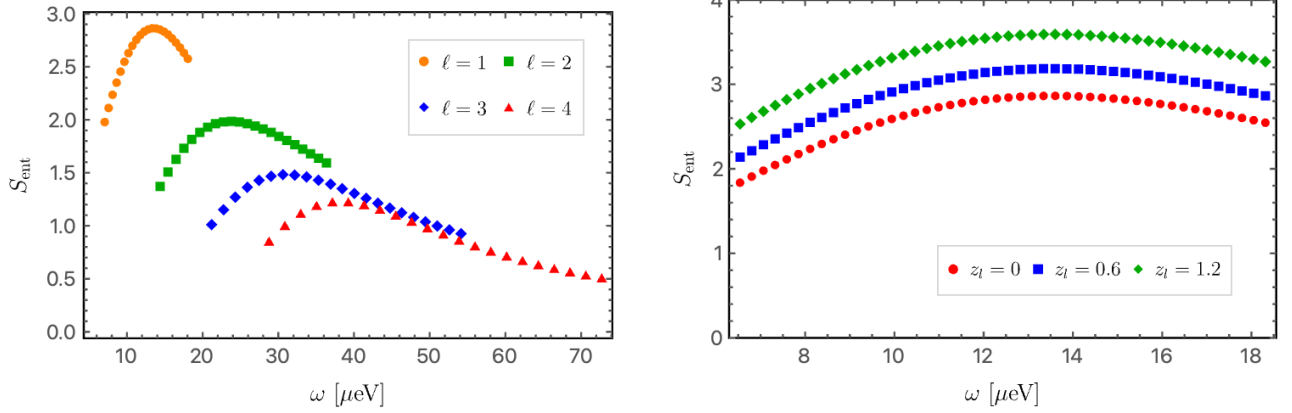


FIG. 7. Entanglement entropy for OUT modes for vacuum input (left) and for a one-mode squeezed input with squeezing intensity z_l for modes with $\ell = 1$ (right) as a function of the frequency. These plots are obtained for a polariton fluid with velocity depicted in Fig. 5. Only frequencies describing propagating superradiant modes are shown.

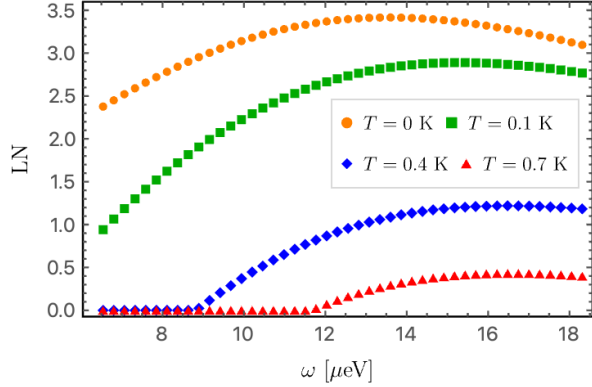


FIG. 8. The LN for OUT modes with $\ell = 1$ under four different thermal input states with varying temperatures. This plot illustrates how the presence of thermal noise degrades entanglement. The frequencies at which LN vanishes are explained by $T_c(\omega, \ell)$ and are also displayed in Fig. 6.

can be achieved using a pure loss channel (see, for example, [39]). In this model, quanta have a probability η of being observed and a probability $(1-\eta)$ of being replaced by the vacuum. The parameter η represents the detection efficiency or parameterizes the coupling to an environmental degree of freedom. This model maintains the Gaussian nature of quantum states. Further details are provided in Appendix B.

Fig. 10 shows the behavior of entanglement in the OUT state, quantified by the LN, as it varies with η . The LN decreases rapidly when η significantly deviates from unity. Entanglement enhances with the squeezing intensity, but this is only notable for high detection efficiency $\eta > 90\%$.

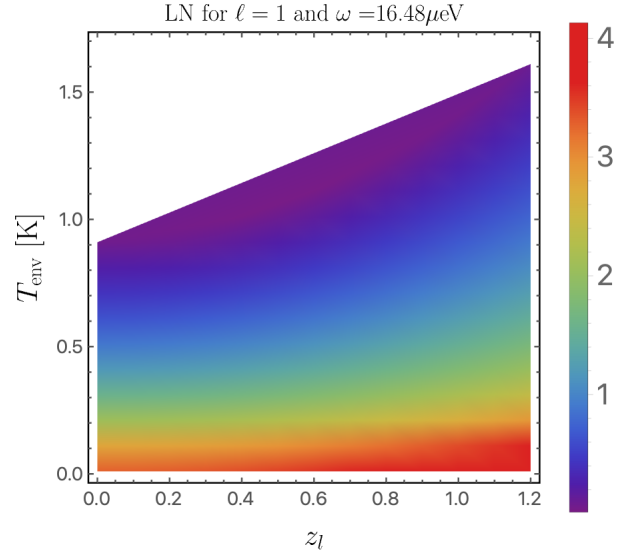


FIG. 9. The LN of the OUT modes as a function of the squeezing intensity of the initial state z_l and the temperature T_{env} . White points have LN=0. The value of the LN is independent of the squeezing angle ϕ_l . The results for other superradiant modes exhibit qualitatively similar behaviors. This figure illustrates the interplay between the detrimental effects of temperature and the amplifying influence of initial squeezing.

VII. EXPERIMENTAL PROPOSAL FOR DETECTION OF ENTANGLEMENT

Thermal noise is a roadblock between any experiment aiming at observing amplification by rotational super-radiance and the resulting generation of entanglement. Specifically, polaritons couple to the vibrations of the crystalline structure of the semiconductor quantum wells. This heat transfer mechanism results in the generation of “heat phonons” (collective excitations) in typical ex-

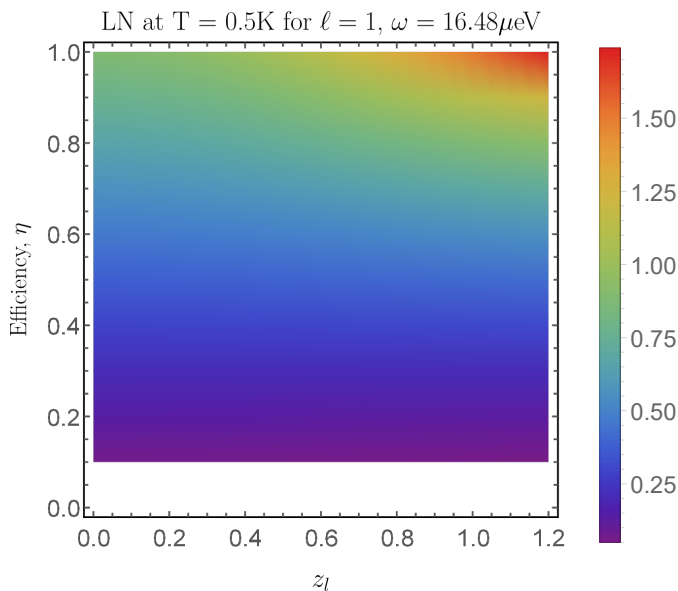


FIG. 10. Variation of entanglement (quantified by LN) between the two OUT modes with the detection efficiency η and the squeezing intensity in the initial state z_l . White points have LN=0.

perimental conditions even at vanishing temperatures, although there is a threshold below which the generation of collective excitations is dominated by the photonic vacuum [42]. However, the data of Fig. 9 indicates that entanglement can be measured at the output even in the presence of thermal noise, provided that a single-mode squeezed state is made to scatter at the ergosurface and that the sample is cooled to low-enough temperatures, which are within the reach of dilution cryostats ($T < 0.3$ K).

The strategy to observe entanglement thus is to send a mode of orbital angular momentum within the superradiance acceptance window, with one squeezed quadrature (either phase or intensity). Orbital angular momentum can be readily obtained by shaping the Gaussian mode of a laser with a spatial light modulator [43]. This can then be used to pump an optical parametric oscillator (OPO). Type-I OPOs regularly yield above 3dB of squeezing below the shot-noise [44] with records at near-infrared wavelengths (as the resonance of the cavity used in our experiment in section IV B) of about 9dB with improved detection methods [45]. These correspond to squeezing intensities of 0.35 and 1.04 respectively.

At the output, intensity correlations and phase anticorrelations can be measured with homodyne detection. This consists of collecting the photons exiting the cavity at a given angle from a given spot, corresponding to excitations spatially located on either side of the ergosurface.⁹ Each of the two beams (which share the same fre-

quency) is then interfered with a (spatially matched) reference beam (local oscillator, LO, provided by the same laser that generated the squeezed state at the input) on a beam-splitter. The resulting interference pattern is measured with photodiodes in both output ports of the beam-splitter, while the relative phase of the signal beams and the LO can be scanned by modulating the path-length of the LO to the beam splitter. This allows for the resolution of both quadratures of the output state and to thus reconstruct its density matrix by optical state tomography [46]. From there, the LN (33) can be evaluated using the analytical tools presented in this article.

VIII. OUTLOOK

Superradiant amplification is a universal phenomenon in which radiation scattered off time-independent potentials exhibits greater amplitude than the incoming radiation. Because of the type of input states commonly used in theoretical and experimental investigations (see the review [14]), superradiance is commonly believed to yield only classical statistics, i.e., classically correlated radiation resulting from the amplification and redistribution of incoming field quanta.

In this paper, we have revisited the basics of superradiance and described its field theoretic origin as the scattering of field modes having opposite symplectic norm Q_{KG} (which is the conserved quantity in relativistic bosonic field theories). From there, we have used tools from the theory of Gaussian quantum bosonic systems to identify that the symplectic transformation describing superradiant scattering is a two-mode squeezer.

From this perspective, superradiance shares similarities with the Hawking effect, since the latter is also described by a two-mode squeezer [47–49]. A key difference is that the pair production from superradiance does not follow a black body spectrum.

As in any two-mode squeezing process, entanglement is not exclusive to vacuum input; rather, it extends to a broad range of input states, including coherent states. However, in the case of coherent states, quantum correlations tend to be drowned by classical correlations. This overshadowing is the origin of the common belief that superradiance only yields classical statistics. We have shown that entanglement generation can be modulated at will, by appropriately choosing the input state: while thermal fluctuations at the input inhibit the generation of entanglement, the use of (unentangled) single-mode squeezed states amplifies the non-separability at the out-

⁹ The angles at which photons come out of the cavity can be determined thanks to coherent probe spectroscopy, where a continuous-wave, coherent state excites collective excitations of the fluid on either side of the ergosurface, yielding their Bogoliubov spectrum [30].

put. These findings establish that superradiance is an entanglement-generating phenomenon.

In the context of rotational superradiance in ergoregions, the superradiant amplification of vacuum fluctuations yields a finite population of negative-norm field excitations in the ergoregion. In the absence of dissipation, repeated superradiant amplification of this negative-norm population would result in a build-up of its amplitude, resulting in a dynamical instability of the ergoregion [20]. In this paper, we have proposed a new configuration to quench the intrinsic dynamical instability of ergoregions. We have experimentally created an irrotational vortex within a polaritonic quantum fluid of light, which has a driven-dissipative dynamics. In numerical simulations, we have shown that superradiance could occur. We explain the stability of the ergoregion observed in numerical simulations as a result of the losses in the system (mostly due to the photonic decay of the cavity).

This configuration with a horizonless ergoregion has allowed us to apply our theoretical methods to the study of quantum emission by rotational superradiance.

We have taken noise and losses into account in our calculations and shown that, although entanglement is generically degraded by thermal noise, it can be recovered using single-mode squeezed states at the input. This strategy can be used in future experiments to facilitate the observation of entanglement generation by superradiance.

In conclusion, our methods permit the study of rotational superradiance with control over the input state,

a feat not attainable in the presence of horizons because of the Hawking effect. This presents a new avenue for both theoretical and experimental exploration of this phenomenon. Nevertheless, our analysis also has implications for rotating configurations where dissipation is provided by a horizon, as for spinning black holes or analogue gravity experiments [18, 19, 50, 51]. Indeed, in scenarios featuring a horizon, the dynamics of entanglement will be ruled by the interplay between the Hawking effect and rotational superradiance [52]. An understanding of this interplay requires knowledge of each of these individual mechanisms. Having the capability to investigate quantum emission originating from each effect independently, becomes valuable in this regard.

ACKNOWLEDGMENTS

We have benefited from discussions with Julio Arcechea, Alberto Bramati, Beatriz Elizaga Navascués, Alessandro Fabbri, Elisabeth Giacobino, Luca Giacomelli, Mathieu Isoard, Dimitrios Kranas, Jorge Pullin and Justin Wilson. I.A., A.D., and P.C. are supported by the NSF grants PHY-2110273, PHY-1903799, and PHY-2206557, by the RCS program of Louisiana Boards of Regents through the grant LEQSF(2023-25)-RD-A-04, and by the Hearne Institute for Theoretical Physics. A.J.B. is supported by the DARPA Young Faculty Award (YFA) Grant No. N660012014029. M.J.J. acknowledges funding from Ile de France DIM Sirteq via project “FOLIAGE”.

-
- [1] R. H. Dicke, Coherence in Spontaneous Radiation Processes, *Phys. Rev.* **93**, 99 (1954).
- [2] Y. B. Zel’dovich, *Zh.Eksp.Teor.Fiz.* **14**, 270 (1971).
- [3] O. Klein, Die Reflexion von Elektronen an einem Potentialsprung nach der relativistischen Dynamik von Dirac, *Z. Phys.* **53**, 157 (1929).
- [4] F. Sauter, Über das Verhalten eines Elektrons im homogenen elektrischen Feld nach der relativistischen Theorie Diracs, *Z. Phys.* **69**, 742 (1931).
- [5] J. S. Schwinger, On gauge invariance and vacuum polarization, *Phys. Rev.* **82**, 664 (1951).
- [6] A. Arvanitaki, S. Dimopoulos, S. Dubovsky, N. Kaloper, and J. March-Russell, String Axiverse, *Phys. Rev. D* **81**, 123530 (2010), [arXiv:0905.4720 \[hep-th\]](https://arxiv.org/abs/0905.4720).
- [7] A. Arvanitaki and S. Dubovsky, Exploring the String Axiverse with Precision Black Hole Physics, *Phys. Rev. D* **83**, 044026 (2011), [arXiv:1004.3558 \[hep-th\]](https://arxiv.org/abs/1004.3558).
- [8] R. Penrose, Gravitational collapse: The role of general relativity, *Riv. Nuovo Cim.* **1**, 252 (1969).
- [9] R. Penrose and R. M. Floyd, Extraction of rotational energy from a black hole, *Nature* **229**, 177 (1971).
- [10] W. H. Press and S. A. Teukolsky, Floating Orbits, Superradiant Scattering and the Black-hole Bomb, *Nature* **238**, 211 (1972).
- [11] S. A. Teukolsky and W. H. Press, Perturbations of a rotating black hole. III - Interaction of the hole with gravitational and electromagnetic radiation, *Astrophys. J.* **193**, 443 (1974).
- [12] R. D. Blandford and R. L. Znajek, Electromagnetic extractions of energy from Kerr black holes, *Mon. Not. Roy. Astron. Soc.* **179**, 433 (1977).
- [13] Y. B. Zel’dovich, *Zh.Eksp.Teor.Fiz.* **62**, 2076 (1972).
- [14] R. Brito, V. Cardoso, and P. Pani, Superradiance – the 2020 Edition, [arXiv:1501.06570 \[astro-ph, physics:gr-qc, physics:hep-ph, physics:hep-th, physics:physics\]](https://arxiv.org/abs/1501.06570) (2020).
- [15] A. A. Starobinskii, Amplification of waves during reflection from a rotating “black hole”, *Sov. Phys. JETP* **64**, 48 (1973).
- [16] W. G. Unruh, Second quantization in the Kerr metric, *Phys. Rev. D* **10**, 3194 (1974).
- [17] J. L. Friedman, Generic instability of rotating relativistic stars, *Commun. Math. Phys.* **62**, 247 (1978).
- [18] T. Torres, S. Patrick, A. Coutant, M. Richartz, E. W. Tedford, and S. Weinfurter, Rotational superradiant scattering in a vortex flow, *Nature Physics* **13**, 833 (2017).
- [19] M.-C. Braidotti, R. Prizia, C. Maitland, F. Marino, A. Prain, I. Starshynov, N. Westerberg, E. M. Wright, and D. Faccio, Measurement of Penrose Superradiance in a Photon Superfluid, *Physical Review Letters* **128**, 013901 (2022).
- [20] J. L. Friedman, Ergosphere instability, *Commun. Math.*

- Phys.* **63**, 243 (1978).
- [21] N. Comins and B. Schutz, On the ergoregion instability, *Proceedings of the Royal Society of London. A. Mathematical and Physical Sciences* **364**, 211 (1978).
- [22] L. Giacomelli and I. Carusotto, Understanding superradiant phenomena with synthetic vector potentials in atomic Bose-Einstein condensates, *Phys. Rev. A* **103**, 043309 (2021), [arXiv:2011.01736 \[cond-mat.quant-gas\]](https://arxiv.org/abs/2011.01736).
- [23] I. Carusotto and C. Ciuti, Quantum fluids of light, *Reviews of Modern Physics* **85**, 10.1103/RevModPhys.85.299 (2013).
- [24] J. Kasprzak, M. Richard, S. Kundermann, A. Baas, P. Jeambrun, J. M. J. Keeling, F. M. Marchetti, M. H. Szymańska, R. André, J. L. Staehli, V. Savona, P. B. Littlewood, B. Deveaud, and L. S. Dang, Bose-Einstein condensation of exciton polaritons, *Nature* **443**, 10.1038/nature05131 (2006).
- [25] R. Balili, V. Hartwell, D. Snoke, L. Pfeiffer, and K. West, Bose-Einstein Condensation of Microcavity Polaritons in a Trap, *Science* **316**, 10.1126/science.1140990 (2007).
- [26] K. G. Lagoudakis, M. Wouters, M. Richard, A. Baas, I. Carusotto, R. André, L. S. Dang, and B. Deveaud-Plédran, Quantized vortices in an exciton-polariton condensate, *Nature Physics* **4**, 10.1038/nphys1051 (2008).
- [27] S. Utsunomiya, L. Tian, G. Roumpos, C. W. Lai, N. Kumada, T. Fujisawa, M. Kuwata-Gonokami, A. Löffler, S. Höfling, A. Forchel, and Y. Yamamoto, Observation of Bogoliubov excitations in exciton-polariton condensates, *Nature Physics* **4**, 700 (2008).
- [28] A. Amo, J. Lefrère, S. Pigeon, C. Adrados, C. Ciuti, I. Carusotto, R. Houdré, E. Giacobino, and A. Bramati, Superfluidity of polaritons in semiconductor microcavities, *Nature Physics* **5**, 805 (2009).
- [29] A. Baas, J. P. Karr, H. Eleuch, and E. Giacobino, Optical bistability in semiconductor microcavities, *Phys. Rev. A* **69**, 023809 (2004).
- [30] F. Claude, M. Jacquet, R. Usciati, I. Carusotto, E. Giacobino, A. Bramati, and Q. Glorieux, High-Resolution Coherent Probe Spectroscopy of a Polariton Quantum Fluid, *Physical Review Letters* **129**, 103601 (2022).
- [31] J. Macher and R. Parentani, Black/white hole radiation from dispersive theories, *Physical Review D* **79**, 124008 (2009).
- [32] M. Visser, Acoustic black holes: horizons, ergospheres and Hawking radiation, *Classical and Quantum Gravity* **15**, 1767 (1998).
- [33] M. J. Jacquet, M. Joly, F. Claude, L. Giacomelli, Q. Glorieux, A. Bramati, I. Carusotto, and E. Giacobino, Analogue quantum simulation of the Hawking effect in a polariton superfluid, *The European Physical Journal D* **76**, 152 (2022).
- [34] S. N. Alperin and N. G. Berloff, Multiply charged vortex states of polariton condensates, *Optica* **8**, 301 (2021).
- [35] A. Peres, Separability criterion for density matrices, *Physical Review Letters* **77**, 1413 (1996).
- [36] G. Vidal and R. F. Werner, Computable measure of entanglement, *Phys. Rev. A* **65**, 032314 (2002).
- [37] M. B. Plenio, Logarithmic negativity: A full entanglement monotone that is not convex, *Physical Review Letters* **95**, 090503 (2005).
- [38] C. Weedbrook, S. Pirandola, R. García-Patrón, N. J. Cerf, T. C. Ralph, J. H. Shapiro, and S. Lloyd, Gaussian quantum information, *Reviews of Modern Physics* **84**, 621 (2012).
- [39] A. Serafini, *Quantum continuous variables: a primer of theoretical methods* (CRC press, 2017).
- [40] S. L. Braunstein, Squeezing as an irreducible resource, *Phys. Rev. A* **71**, 055801 (2005).
- [41] J. K. Asbóth, J. Calsamiglia, and H. Ritsch, Computable Measure of Nonclassicality for Light, *Phys. Rev. Lett.* **94**, 173602 (2005).
- [42] I. Frérot, A. Vashisht, M. Morassi, A. Lemaître, S. Ravets, J. Bloch, A. Minguzzi, and M. Richard, Bogoliubov excitations driven by thermal lattice phonons in a quantum fluid of light, [arXiv:2304.08677](https://arxiv.org/abs/2304.08677) (2023).
- [43] V. Parigi, V. D'Ambrosio, C. Arnold, L. Marrucci, F. Sciarrino, and J. Laurat, Storage and retrieval of vector beams of light in a multiple-degree-of-freedom quantum memory, *Nature Communications* **6**, 7706 (2015).
- [44] L.-A. Wu, H. J. Kimble, J. L. Hall, and H. Wu, Generation of squeezed states by parametric down conversion, *Phys. Rev. Lett.* **57**, 2520 (1986).
- [45] Y. Takeno, M. Yukawa, H. Yonezawa, and A. Furusawa, Observation of -9 db quadrature squeezing with improvement of phase stability in homodyne measurement, *Opt. Express* **15**, 4321 (2007).
- [46] A. I. Lvovsky and M. G. Raymer, Continuous-variable optical quantum-state tomography, *Rev. Mod. Phys.* **81**, 299 (2009).
- [47] I. Agullo, A. J. Brady, and D. Kranas, Quantum Aspects of Stimulated Hawking Radiation in an Optical Analog White-Black Hole Pair, *Phys. Rev. Lett.* **128**, 091301 (2022), [arXiv:2107.10217 \[gr-qc\]](https://arxiv.org/abs/2107.10217).
- [48] A. J. Brady, I. Agullo, and D. Kranas, Symplectic circuits, entanglement, and stimulated Hawking radiation in analogue gravity, *Phys. Rev. D* **106**, 105021 (2022), [arXiv:2209.11317 \[gr-qc\]](https://arxiv.org/abs/2209.11317).
- [49] I. Agullo, A. J. Brady, and D. Kranas, Event horizons are tunable factories of quantum entanglement, *Int. J. Mod. Phys. D* **31**, 2242008 (2022), [arXiv:2209.09980 \[gr-qc\]](https://arxiv.org/abs/2209.09980).
- [50] M. J. Jacquet, T. Boulier, F. Claude, A. Maître, E. Cancellieri, C. Adrados, A. Amo, S. Pigeon, Q. Glorieux, A. Bramati, and E. Giacobino, Polariton fluids for analogue gravity physics, *Philosophical Transactions of the Royal Society A*: **378**, 20190225 (2020).
- [51] P. Švančara, P. Smaniotto, L. Solidoro, J. F. MacDonald, S. Patrick, R. Gregory, C. F. Barenghi, and S. Weinfurter, *Exploring the Quantum-to-Classical Vortex Flow: Quantum Field Theory Dynamics on Rotating Curved Spacetimes* (2023).
- [52] I. Agullo, A. J. Brady, A. Delhom, and D. Kranas, Entanglement from rotating black holes in thermal baths, (2023), [arXiv:2307.06215 \[gr-qc\]](https://arxiv.org/abs/2307.06215).
- [53] R. M. Wald, *Quantum Field Theory in Curved Space-Time and Black Hole Thermodynamics*, Chicago Lectures in Physics (University of Chicago Press, Chicago, IL, 1995).
- [54] S. Patrick, Rotational superradiance with Bogoliubov dispersion, [arXiv:2011.04620 \[cond-mat, physics:gr-qc, physics:physics\]](https://arxiv.org/abs/2011.04620) (2020).

Appendix A: Proof of the theorem characterizing superradiance

To prove this theorem, we will actually prove its negation: the scattering is not superradiant if and only if \mathbf{B} is unitary.

Firstly, since

$$\mathbf{B}^\dagger \cdot \mathbf{B} = \begin{pmatrix} |T|^2 + |R|^2 & T^*r + R^*t \\ Tr^* + Rt^* & |r|^2 + |t|^2 \end{pmatrix}, \quad (\text{A1})$$

unitarity of \mathbf{B} requires the following constraints

$$|T|^2 + |R|^2 = 1, \quad |t|^2 + |r|^2 = 1 \quad \text{and} \quad Tr^* + Rt^* = 0, \quad (\text{A2})$$

implying that $|T|, |R|, |t|$ and $|r|$ are all smaller than unity and the scattering is non-superradiant.

To prove that non-superradiant scattering implies unitarity of \mathbf{B} , let us use the conserved quantity Q_{KG} to define a (non-positive definite) Hermitian inner product in the space of complex solutions to the Klein-Gordon equation

$$\langle W_1, W_2 \rangle \equiv Q_{\text{KG}}(W_1, W_2) = i/\hbar \int (W_1^* \partial_t W_2 - \partial_t W_1^* W_2) dx, \quad (\text{A3})$$

This is commonly referred to as the Klein-Gordon or symplectic product (see, e.g., [53]). Without loss of generality, we can work with wave packets normalized to have $Q_{\text{KG}} = \pm 1$. Furthermore, it is easy to check that left- and right-moving wave packets are orthogonal. With this, conservation of Q_{KG} implies

$$\begin{aligned} \langle W_r^{\text{in}}, W_r^{\text{in}} \rangle &= |T|^2 \langle W_r^{\text{out}}, W_r^{\text{out}} \rangle + |R|^2 \langle W_l^{\text{out}}, W_l^{\text{out}} \rangle \\ \langle W_l^{\text{in}}, W_l^{\text{in}} \rangle &= |r|^2 \langle W_r^{\text{out}}, W_r^{\text{out}} \rangle + |t|^2 \langle W_l^{\text{out}}, W_l^{\text{out}} \rangle \\ \langle W_r^{\text{in}}, W_l^{\text{in}} \rangle &= T^*r \langle W_r^{\text{out}}, W_r^{\text{out}} \rangle + R^*t \langle W_l^{\text{out}}, W_l^{\text{out}} \rangle. \end{aligned} \quad (\text{A4})$$

For a non-superradiant scattering, $|T|, |R|, |t|$ and $|r|$ are all smaller than unity. With this, relations (A4) imply that the KG norm of each of the four wave packets must have the same sign, either +1 or -1. Furthermore, (A4) also implies

$$|T|^2 + |R|^2 = 1, \quad |t|^2 + |r|^2 = 1 \quad \text{and} \quad Tr^* + Rt^* = 0, \quad (\text{A5})$$

implying that \mathbf{B} is a unitary matrix. This proves the theorem.

We conclude this appendix by presenting several expressions employed in the main text. It has been established that, in the context of non-superradiant scattering, all four modes participating in the scattering process exhibit the same sign of Q_{KG} . In contrast, in superradiant scattering scenarios, the two IN modes bear different signs of Q_{KG} , and the same applies to the two OUT modes.

When, for superradiant scattering, $\langle W_r^{\text{in}}, W_r^{\text{in}} \rangle = \langle W_r^{\text{out}}, W_r^{\text{out}} \rangle$, the Eqns. (A4) lead to the following constraints

$$|T|^2 - |R|^2 = 1, \quad |t|^2 - |r|^2 = 1 \quad \text{and} \quad Tr^* - Rt^* = 0. \quad (\text{A6})$$

And, for superradiant scattering and $\langle W_r^{\text{in}}, W_r^{\text{in}} \rangle = -\langle W_r^{\text{out}}, W_r^{\text{out}} \rangle$, Eqns. (A4) produce

$$|R|^2 - |T|^2 = 1, \quad |r|^2 - |t|^2 = 1 \quad \text{and} \quad Tr^* - Rt^* = 0. \quad (\text{A7})$$

These two sets of constraints indicate that either reflection or transmission coefficients (or both) have an absolute value greater than one, indicating superradiant scattering.

Appendix B: Gaussian states, entanglement quantifiers, and entanglement witnesses

This appendix contains a brief summary of techniques of Gaussian states for bosonic quantum systems on which we have based the calculations in the main body of the paper. These are well-known tools, and detailed descriptions of them can be found, for instance, in [38, 39]. In comparing the content of this appendix with other references, including [38, 39], the reader should bear in mind that we work here with creation and annihilation operators, rather than Hermitian combinations of them. This introduces some differences in the expressions we write below.

A bosonic quantum system with N degrees of freedom can be described in terms of $2N$ creation and annihilation operators $\mathbf{A} = (a_1, \dots, a_N, a_1^\dagger, \dots, a_N^\dagger)$ which satisfy standard commutation relations

$$[\hat{A}^I, \hat{A}^J] = \Omega^{IJ}, \quad \text{where} \quad \Omega := \begin{pmatrix} 0_N & \mathbb{I}_N \\ -\mathbb{I}_N & 0_N \end{pmatrix} \quad (\text{B1})$$

is the symplectic form and $I, J \in \{1, \dots, 2N\}$. A general state for such system will be characterized by a density matrix $\hat{\rho}$, which encodes the information of the infinitely many moments of the creation and annihilation operators

$$\langle \hat{A}^{I_1} \dots \hat{A}^{I_n} \rangle := \text{Tr}[\hat{\rho} \hat{A}^{I_1} \dots \hat{A}^{I_n}], \quad (\text{B2})$$

with $n \in \mathbb{N}$. Of special relevance for us are the first and the (symmetrized and centered) second moments, known as mean vector and covariance matrix, whose components are respectively

$$\mu^I = \langle \hat{A}^I \rangle \quad \sigma^{IJ} = \langle \{\hat{A}^I - \mu^I, \hat{A}^J - \mu^J\} \rangle, \quad (\text{B3})$$

where curly brackets denote anti-commutator. Among all possible quantum states, there is a subset called Gaussian states, which have the remarkable property that all their moments can be written in terms of their first and second moments, in analogy to what occurs for Gaussian probability distributions. Hence, these states are fully characterized by their mean and covariance matrix, which contain complete information on the physical properties of the state. Furthermore, Gaussian states are ubiquitous, with prominent examples being the ground or thermal states for any quadratic Hamiltonian, and any state that can be prepared by applying symplectic transformations to such states. As example, the vacuum is characterized by

$$\mu_{\text{vac}} = \mathbf{0} \quad \text{and} \quad \sigma_{\text{vac}} = \begin{pmatrix} 0_N & \mathbb{I}_N \\ \mathbb{I}_N & 0_N \end{pmatrix}, \quad (\text{B4})$$

a coherent state is characterized by having the same covariance matrix as the vacuum but a “displaced” mean, namely $\mu_{\text{coh}} \neq \mathbf{0}$ and $\sigma_{\text{coh}} = \sigma_{\text{vac}}$. A thermal state is of the form $\mu = \mathbf{0}$ and $\sigma = \oplus_j (1 + 2n_j) \sigma_{\text{vac}}$, where n_j is the mean number of quanta in the mode j , with $j \in \{1, \dots, N\}$, and the covariance matrix in the direct sum are those corresponding to a vacuum 1-mode system.

Furthermore, if an N -mode system is in a Gaussian state, the reduced state of any subset of the N modes is also Gaussian.

The evolution of linear quantum systems —i.e., systems described by a Hamiltonian at most quadratic in the creation and annihilation operators— is completely determined by the classical evolution. Hence, evolution can be encoded in a linear symplectic transformation \mathbf{S} . These are $2N \times 2N$ complex matrices of the form

$$\mathbf{S} = \begin{pmatrix} \boldsymbol{\alpha} & \boldsymbol{\beta} \\ \boldsymbol{\beta}^* & \boldsymbol{\alpha}^* \end{pmatrix}, \quad (\text{B5})$$

with $\boldsymbol{\alpha}$ and $\boldsymbol{\beta}$ complex $N \times N$ matrices, and satisfying that they leave invariant the symplectic form, i.e., $\mathbf{S} \cdot \Omega \cdot \mathbf{S}^\top = \Omega$. This condition implies

$$\boldsymbol{\alpha} \cdot \boldsymbol{\alpha}^\dagger - \boldsymbol{\beta} \cdot \boldsymbol{\beta}^\dagger = \mathbb{I}_2, \quad \boldsymbol{\alpha} \cdot \boldsymbol{\beta}^\top - \boldsymbol{\beta} \cdot \boldsymbol{\alpha}^\top = 0_2, \quad (\text{B6})$$

Matrices \mathbf{S} of this form constitute a group isomorphic to the symplectic group $\text{Sp}(2N, \mathbb{R})$.

Moreover, linear evolution preserves Gaussianity. If the initial state at time t_0 is Gaussian and characterized by $\mu_{t_0}^i$ and $\sigma_{t_0}^{ij}$, the state of the system will be Gaussian at all times, and given by $\mu_t^i = S^i_k \mu_{t_0}^k$ and $\sigma_t^{ij} = S^i_k \sigma_{t_0}^{km} S^j_m$, or, in matrix notation

$$\boldsymbol{\mu}_t = \mathbf{S} \cdot \boldsymbol{\mu}_{t_0} \quad \text{and} \quad \boldsymbol{\sigma}_t = \mathbf{S} \cdot \boldsymbol{\sigma}_{t_0} \cdot \mathbf{S}^\top. \quad (\text{B7})$$

In the Heisenberg picture, this evolution is translated to the creation and annihilation operators as

$$\mathbf{A}_t = \mathbf{S} \cdot \mathbf{A}_{t_0}. \quad (\text{B8})$$

Because \mathbf{S} is symplectic, this transformation preserves the standard commutation relations written in (B2).

We can express the mean number of quanta in a given mode i as

$$\langle \hat{N}_i \rangle = \frac{1}{2} \sigma^{i, i+N} + \mu^i \mu^{i+N} - \frac{1}{2}, \quad (\text{B9})$$

We use this expression to compute the number of quanta for the cases considered in Eqs. (13) to (17). Starting with the vacuum case, we have an initial state characterized by (B11) for $N = 2$, and the matrix \mathbf{S} describing superradiant scattering (Eqn. (11) in the main text)

$$\mathbf{S}_{\text{SR}} = \begin{pmatrix} T & 0 & 0 & r \\ 0 & t^* & R^* & 0 \\ 0 & r^* & T^* & 0 \\ R & 0 & 0 & t \end{pmatrix}. \quad (\text{B10})$$

The state after the scattering is

$$\boldsymbol{\mu}_{\text{out}} = \mathbf{S} \cdot \boldsymbol{\mu}_{\text{vac}} = \mathbf{0} \quad \text{and} \quad \boldsymbol{\sigma}_{\text{out}} = \mathbf{S} \cdot \boldsymbol{\sigma}_{\text{vac}} \cdot \mathbf{S}^\top = \begin{pmatrix} 0 & TR^* + rt^* & 1 + 2|R|^2 & 0 \\ TR^* + rt^* & 0 & 0 & 1 + 2|R|^2 \\ 1 + 2|R|^2 & 0 & 0 & RT^* + r^*t \\ 0 & 1 + 2|R|^2 & r^*t + RT^* & 0 \end{pmatrix}, \quad (\text{B11})$$

where we have used $|T|^2 = 1 + |R|^2$, $|r| = |R|$ and $|t| = |T|$. Using Eqn. (B9), we find the mean numbers of quanta are

$$\langle \hat{N}_r^{\text{out}} \rangle = \frac{1}{2}(\sigma_{\text{out}}^{13} - 1) = |R|^2 \quad \text{and} \quad \langle \hat{N}_\ell^{\text{out}} \rangle = \frac{1}{2}(\sigma_{\text{out}}^{24} - 1) = |R|^2. \quad (\text{B12})$$

Starting now with a coherent input $|\gamma_r, \gamma_\ell\rangle$, with mean $\boldsymbol{\mu}_{\text{coh}} = (\gamma_r, \gamma_\ell, \gamma_r^*, \gamma_\ell^*)^\top$ and same covariance matrix as the vacuum, we find that

$$\boldsymbol{\mu}_{\text{out}} = (T\gamma_r + r\gamma_\ell^*, t^*\gamma_\ell + R^*\gamma_r^*, \gamma_\ell r^* + T^*\gamma_r^*, R\gamma_r + t\gamma_\ell^*)^\top, \quad (\text{B13})$$

and the $\boldsymbol{\sigma}_{\text{out}}$ given in (B11). Thus, we find

$$\langle \hat{N}_r^{\text{out}} \rangle = \frac{1}{2}(\sigma_{\text{out}}^{13} - 1) + \mu_{\text{out}}^1 \mu_{\text{out}}^3 = \underbrace{|\gamma_r|^2}_{\text{initial}} + \underbrace{|R|^2}_{\text{vacuum}} + \underbrace{|R|^2(|\gamma_r|^2 + |\gamma_\ell|^2) + 2\text{Re}[r^*T\gamma_r\gamma_\ell]}_{\text{stimulated}}, \quad (\text{B14})$$

$$\langle \hat{N}_\ell^{\text{out}} \rangle = \frac{1}{2}(\sigma_{\text{out}}^{24} - 1) + \mu_{\text{out}}^2 \mu_{\text{out}}^4 = \underbrace{|\gamma_\ell|^2}_{\text{initial}} + \underbrace{|R|^2}_{\text{vacuum}} + \underbrace{|R|^2(|\gamma_\ell|^2 + |\gamma_r|^2) + 2\text{Re}[t^*R\gamma_\ell\gamma_r]}_{\text{stimulated}}. \quad (\text{B15})$$

These are the expressions given in expressions (14) and (15) in the main text.

Finally, a single-mode squeezed state is a Gaussian state input characterized by $\boldsymbol{\mu}_{\text{sq}} = 0$ and

$$\boldsymbol{\sigma}_{\text{sq}} = \begin{pmatrix} -e^{i\phi_l} \sinh 2z_l & 0 & \cosh 2z_l & 0 \\ 0 & 0 & 0 & 1 \\ \cosh 2z_l & 0 & -e^{-i\phi_l} \sinh 2z_l & 0 \\ 0 & 1 & 0 & 0 \end{pmatrix}, \quad (\text{B16})$$

where we have squeezed only the first mode. $z_l \in \mathbb{R}$ is called the squeezing intensity, and $\phi_l \in \mathbb{R}$ the squeezing angle.

Starting from this state, we find the state after superradiant scattering is characterized by $\boldsymbol{\mu}_{\text{out}} = 0$ and

$$\boldsymbol{\sigma}_{\text{out}} = \begin{pmatrix} -e^{i\phi_l} T^2 \sinh 2z_l & rt^* + TR^* \cosh 2z_l & |R|^2 + (1 + |R|^2) \cosh 2z_l & -e^{i\phi_l} TR \sinh 2z_l \\ rt^* + TR^* \cosh 2z_l & -e^{-i\phi_l} R^{*2} \sinh 2z_l & -e^{-i\phi_l} R^* T^* \sinh 2z_l & 1 + |R|^2(1 + \cosh 2z_l) \\ |R|^2 + (1 + |R|^2) \cosh 2z_l & -e^{-i\phi_l} R^* T^* \sinh 2z_l & -e^{-i\phi_l} T^{*2} \sinh 2z_l & RT^* + r^*t \\ -e^{i\phi_l} TR \sinh 2z_l & 1 + 2|R|^2 & r^*t + RT^* & -e^{i\phi_l} R^2 \sinh 2z_l \end{pmatrix}. \quad (\text{B17})$$

Again, using formula (B9) to compute the number of particles in each mode, we find

$$\langle \hat{N}_r^{\text{out}} \rangle = \frac{1}{2}(\sigma_{\text{out}}^{13} - 1) = \underbrace{\sinh^2 z_l}_{\text{initial}} + \underbrace{|R|^2}_{\text{vacuum}} + \underbrace{|R|^2 \sinh^2 z_l}_{\text{stimulated}}, \quad (\text{B18})$$

$$\langle \hat{N}_\ell^{\text{out}} \rangle = \frac{1}{2}(\sigma_{\text{out}}^{24} - 1) = \underbrace{|R|^2}_{\text{vacuum}} + \underbrace{|R|^2 \sinh^2 z_l}_{\text{stimulated}}, \quad (\text{B19})$$

which correspond to formulas (16) and (17) in the main text.

Many properties of the state can be extracted from $\boldsymbol{\sigma}$ alone. For instance, the absolute value of the eigenvalues of $\boldsymbol{\sigma} \cdot \boldsymbol{\Omega}^{-1}$ is always greater or equal to 1, and the state is pure if and only if all of these eigenvalues are equal to ± 1 .

For Gaussian states, the information in $\boldsymbol{\sigma}$ is also enough to compute the von Neumann entropy of the state and the Logarithmic Negativity (LN) associated with any bi-partition of the system. These are quantities that we have used to quantify the entanglement generated by superradiance.

The computation of these quantities from the covariance matrix of a given Gaussian state proceeds as follows. The von Neumann entropy of a Gaussian state is given by (see, e.g. [39])

$$S[\boldsymbol{\sigma}] = \sum_k^N \left[\left(\frac{\nu_k + 1}{2} \right) \ln \left(\frac{\nu_k + 1}{2} \right) - \left(\frac{\nu_k - 1}{2} \right) \ln \left(\frac{\nu_k - 1}{2} \right) \right], \quad (\text{B20})$$

where ν_k are the so-called symplectic eigenvalues of the covariance matrix $\boldsymbol{\sigma}$, namely the modulus of the eigenvalues of $\boldsymbol{\sigma} \cdot \boldsymbol{\Omega}^{-1}$. There are only N such eigenvalues, even though these matrices are $2N$ -dimensional, because eigenvalues come in pairs, with the members of each pair differing by a sign. This sign is irrelevant since ν_k are defined as the modulus of the eigenvalues.

Similarly, given Gaussian state $(\boldsymbol{\mu}_{AB}, \boldsymbol{\sigma}_{AB})$, where A and B are subsystems, the Logarithmic Negativity can be computed from the symplectic eigenvalues of the so-called partially transposed state [36, 37], where the transpose is taken with respect to either of the two subsystems. If subsystem A consists of p modes, labeled by $\{k_1, \dots, k_p\}$, with $k_j \in \{1, \dots, N\}$ and $1 \leq p \leq N - 1$, the partially transposed state with respect to A is the Gaussian state with the same mean $\boldsymbol{\mu}_{AB}$ but covariance matrix $\tilde{\boldsymbol{\sigma}}_{AB}$ obtained from $\boldsymbol{\sigma}_{AB}$ just by swapping the rows k_j and k_{j+N} and the columns k_j and k_{j+N} for all the modes of the subsystem A . The Logarithmic Negativity of the bi-partition AB in state $\boldsymbol{\sigma}_{AB}$ is thus given by the formula

$$\text{LogNeg}[\boldsymbol{\sigma}_{AB}] = \sum_i \text{Max}[0, -\log_2 \tilde{\nu}_i] \quad (\text{B21})$$

where $\tilde{\nu}_i^p$ are the symplectic eigenvalues of $\tilde{\boldsymbol{\sigma}}_{AB}$.

Modeling loss

In this subsection, we provide some additional details of the loss model used in section VI.

A simple theory to model loss of a bosonic mode \hat{a} is given by the simple input-output relation $\hat{a} \rightarrow \sqrt{\eta} \hat{a} + \sqrt{1 - \eta} \hat{e}$, where $0 \leq \eta \leq 1$ is the transmittance and \hat{e} is the annihilation operator of an environment mode following thermal Gaussian statistics—i.e., with mean zero, $\langle \hat{e} \rangle = 0$, and variance determined by the thermal population, $\langle \hat{e}^\dagger \hat{e} \rangle = n_{\text{env}}$. To illustrate the model with a short example, consider a strong classical wave, i.e., a coherent state, with intensity (mean number of quanta) $I_{\text{in}} \gg n_{\text{env}}$. The output intensity is then $I_{\text{in}} \rightarrow I_{\text{out}} = \eta I_{\text{in}} + (1 - \eta) n_{\text{env}} \approx \eta I_{\text{in}}$. In other words, the input intensity is attenuated by an amount η . This model is often employed to represent detector losses, where the efficiency of the detector, expressed as a percentage, is $100 \times \eta$.

For simplicity, we consider “pure loss”, such that $n_{\text{env}} = 0$, i.e. the environment is close to the vacuum. On Gaussian states, the pure loss channel transforms the mean and the covariance matrix via

$$\begin{aligned} \boldsymbol{\mu} &\rightarrow \sqrt{\eta} \boldsymbol{\mu} \\ \boldsymbol{\sigma} &\rightarrow \eta \boldsymbol{\sigma} + (1 - \eta) \boldsymbol{\sigma}_{\text{vac}}, \end{aligned} \quad (\text{B22})$$

where $\boldsymbol{\sigma}_{\text{vac}}$ is the covariance matrix of the vacuum. This transformation reflects the fact that quanta make it to the detector with probability η : for $\eta = 0$, all quanta are lost and only the vacuum remains, whilst $\eta = 1$ corresponds to perfect collection of the outgoing radiation.

Appendix C: Kinematics of collective excitations in rotating polariton fluids

In this appendix, we study the kinematics of collective excitations—which are described by a Klein-Gordon field—on the effective curved geometry created by the mean-field of the fluid.

The equation of linear perturbations $\delta\psi$ around the background fluid described by ψ^0 satisfying the stationary equation (19) is

$$i(\partial_t + \mathbf{v}^0 \cdot \nabla) \delta\psi = \left[-\frac{\hbar}{2m_{LP}} \nabla^2 - \frac{i\hbar}{2m_{LP}} (\nabla \cdot \mathbf{v}^0) - \delta + 2gn^0 - i\frac{\gamma}{2} \right] \delta\psi + gn^0 \delta\psi^*, \quad (\text{C1})$$

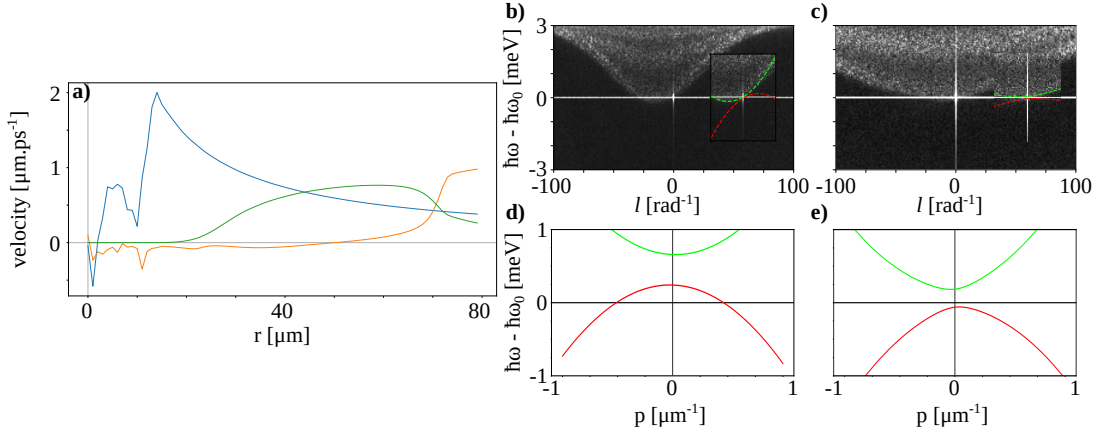


FIG. 11. Collective excitation in the inhomogeneous fluid. **a)** Velocities along a radial cut in Fig. 4 f). Green, c_s ; orange, v_r ; blue, v_θ . **b)** $m - \omega$ dispersion in the supersonic region. **c)** $m - \omega$ dispersion in the subsonic region. Insets: zoom near $m = 0 - \omega = 0$ and fit of WKB dispersion. Green, positive-norm branch; red, negative-norm branch. **d)** $p - \omega$ WKB dispersion in the subsonic region. **e)** $p - \omega$ WKB dispersion in the supersonic region.

where n^0 and \mathbf{v}^0 are the mean-field density and flow velocity, respectively. δ is the effective frequency detuning between the laser and the lower polariton branch at k . Eqn (C1) can be rewritten as a system of linear equations for the fields ϕ and ϕ^* as

$$i(\partial_t + \mathbf{v}^0 \cdot \nabla) \begin{pmatrix} \delta\psi \\ \delta\psi^* \end{pmatrix} = \mathcal{L} \begin{pmatrix} \delta\psi \\ \delta\psi^* \end{pmatrix} = \begin{pmatrix} A & gn^0 \\ -gn^0 & -A^* \end{pmatrix} \begin{pmatrix} \delta\psi \\ \delta\psi^* \end{pmatrix} \quad (\text{C2})$$

where $A = -\frac{\hbar}{2m_{LP}}\nabla^2 - \frac{i\hbar}{2m_{LP}}(\nabla \cdot \mathbf{v}^0) - \delta + 2gn^0 - i\frac{\gamma}{2}$.

In time-independent backgrounds, modes with different frequencies decouple, and Eqn (C2) turns into an eigenvalue problem for the differential operator \mathcal{L} . If the background is also homogeneous, the modes can be expanded in plane waves with fluid-rest-frame wavevector \mathbf{k} , yielding the Bogoliubov dispersion relation [23]

$$\omega - \mathbf{v}^0 \cdot \mathbf{k} = -\frac{i\gamma}{2} \pm \sqrt{\frac{\hbar^2 k^4}{4m_{LP}^2} + \frac{\hbar k^2}{m_{LP}}(2gn^0 - \delta) + (gn^0 - \delta)(3gn^0 - \delta)}. \quad (\text{C3})$$

In this driven-dissipative system, the frequency detuning δ controls a mass gap in the dispersion (which vanishes only if $\delta = gn^0, 3gn^0$).

While Eqn (C3) describes well the spectrum of collective excitations in configurations without rotation in which plane waves are the eigenfunctions of the system [30], this is not the case when working with configurations with rotational symmetry around an axis. In that case, the basis is best obtained by decomposing in the eigenfunctions of the angular momentum operator $L_\theta = -i\partial/\partial\theta$, which have the form $e^{i\ell\theta}$ with eigenvalue ℓ , and which will not mix during the evolution.

In the rest frame of the fluid (where $\partial_{\vec{t}} = 0$), the problem is solved by finding eigenfunctions of the operator \mathcal{L} . For a given ℓ , these are the eigenfunctions of both the Laplacian operator ∇^2 and the angular momentum operator L_θ and are of the form $e^{i\ell\theta} J_\ell(pr), e^{i\ell\theta} Y_\ell(pr)$ (J_ℓ and Y_ℓ are Bessel functions). Their eigenvalues are $-p^2$.

Bessel functions do asymptotically approach radial phase waves (their amplitude has an oscillatory wave-like profile), but as they approach an ℓ - and p -dependent radius r_0 (r_0 increases with ℓ and reduces with p), their amplitude starts decaying, much like evanescent waves. (Physically, this can be thought of as a consequence of the effective centrifugal potential barrier, which diverges as $r \rightarrow 0$). So the label p is not a plane-wave wavevector. Yet, it is possible to arrive at a ‘‘dispersion relation’’ for a profile with vanishing radial velocity:

$$\omega - \frac{v_\theta \ell}{r} = -\frac{i\gamma}{2} \pm \sqrt{\frac{\hbar^2 p^4}{4m_{LP}^2} + \frac{\hbar p^2}{m_{LP}}(2gn^0 - \delta) + (gn^0 - \delta)(3gn^0 - \delta)}. \quad (\text{C4})$$

Using the WKB approximation, Eqn (C3) can be adapted, with $\mathbf{k} = (p, \ell/r)$, to recover an expression in which the labels can be physically interpreted as usual [54]. The resulting ℓ -dependent terms that do not vanish in the $p \rightarrow 0$ limit yield a position- and ℓ -dependent contribution to the mass gap in the spectrum of cylindrical waves,

which effectively accounts for the effect of the centrifugal barrier near the origin (locally evanescent amplitudes). In the hydrodynamical approximation, neglecting cavity losses and with $v_r = 0$, the WKB dispersion is

$$\omega - \frac{v_\theta \ell}{r} = \pm c_s \sqrt{p^2 + \frac{\ell^2}{r^2}}. \quad (\text{C5})$$

From Eqn (C5), we find the condition for positive-(negative-)norm modes to propagate (be real-valued k , ω roots) at positive laboratory-frame frequency at a given radius r_0 :

$$\omega - \frac{v_\theta(r_0)\ell}{r_0} > \frac{c_s \ell}{r_0} \quad \text{and} \quad \omega - \frac{v_\theta(r_0)\ell}{r_0} < -\frac{c_s \ell}{r_0}, \quad (\text{C6})$$

respectively.

We now study the spectrum of collective excitations. We use the Truncated Wigner approximation to add small amplitude noise at all spatial and temporal frequencies to the numerical simulation of the GPE (18). This noise creates collective excitations at resonant-frequencies in the fluid.

Fig. 11 shows the dispersion of collective excitations on either side of the ergosurface. In numerical simulations, after having reached the steady-state of the GPE (18), we subtract the mean-field background and perform angular and temporal Fourier transforms inside r -windows to obtain the local noise spectrum in the $\ell - \omega$ plane. We plot spectra at radii **b**) inside ($r = 25 \mu\text{m}$) and **c**) outside ($r = 67 \mu\text{m}$) the ergoregion. The vortex mean-field is still visible as a vertical spike at $\ell_{vortex} = 0$ (ℓ and \mathbf{p} are defined in the rest frame of the fluid). We observe that the positive-norm branch is more visible than the negative-norm branch.

Insets show zooms on the azimuthal numbers near ℓ_{vortex} , to which the dispersion obtained by the WKB approximation is superimposed (green, positive-norm branch; red, negative-norm branch). The WKB dispersion describes well the noise spectrum over regions where the density is high enough for nonlinear self-interactions. As explained above, modes with $\ell > 0$ have an ℓ/r -dependent mass gap induced by the fluid rotation. This has also been evidenced in experiments in superfluid helium [51].

We also calculate the dispersion (C3) in the laboratory frame for modes with $\ell = 10$ at the same two radii with the WKB approximation ($\delta \neq gn^0$ as in the experiment). We remark that, due to the finite gap inside and outside the ergosurface, there are intervals in which we find no real roots at positive laboratory-frame frequencies on either side of the interface. As explained above, this signals the presence of evanescent waves in these regions [54].

We see that the increase in v_θ across the ergosurface pulls the negative-norm branch to positive frequency, signaling the possibility to excite negative-energy modes and to have superradiant scattering. And indeed, there is a narrow positive-frequency interval for which there are positive-norm mode solutions outside, and negative-norm mode solutions inside the ergosurface. Note that, because of the finite lifetime of polaritons, the group velocity of these rightward and leftward propagating modes has to be taken into account when characterizing the scattering coefficients across the ergosurface — this defines their mean-free path as well as amplitude dampening before and after the scattering process has occurred.

Appendix D: Calculation of the S matrix

Our goal is to obtain, for each mode (ω, ℓ) , the coefficients $T_{\omega\ell}$, $R_{\omega\ell}$, $t_{\omega\ell}$ and $r_{\omega\ell}$ defined from these two scattering processes of wave packets (see Fig. 1 for an illustration)

$$\begin{aligned} W_r^{\text{in}} &\rightarrow T_{\omega\ell} W_r^{\text{out}} + R_{\omega\ell} W_l^{\text{out}}, \\ W_l^{\text{in}} &\rightarrow t_{\omega\ell} W_l^{\text{out}} + r_{\omega\ell} W_r^{\text{out}}. \end{aligned} \quad (\text{D1})$$

Because of the time-independence and rotational symmetry of the problem, the calculation reduces to solve an ordinary differential equation in the radial direction (Eqn. (24)). We proceed as follows.

Eqn. (30) contains the (asymptotic) form of our basis of IN and OUT modes near r_{\min} and r_{\max}

$$\begin{aligned} \varphi_r^{\text{in}}(r_{\min}) &= N_{\omega\ell} \exp \left\{ i \left(\frac{\omega r_{\min}}{c} - \frac{\ell v_\theta(r_{\min})}{c_s} \log \frac{r}{r_{\min}} \right) \right\}, \\ \varphi_l^{\text{in}}(r_{\max}) &= \tilde{N}_{\omega\ell} \exp \left\{ -i \left(\frac{\omega r_{\max}}{c} - \frac{\ell v_\theta(r_{\max})}{c_s} \log \frac{r}{r_{\max}} \right) \right\}, \\ \varphi_r^{\text{out}}(r_{\max}) &= \tilde{N}_{\omega\ell} \exp \left\{ i \left(\frac{\omega r_{\max}}{c} - \frac{\ell v_\theta(r_{\max})}{c_s} \log \frac{r}{r_{\max}} \right) \right\}, \\ \varphi_l^{\text{out}}(r_{\min}) &= N_{\omega\ell} \exp \left\{ -i \left(\frac{\omega r_{\min}}{c} - \frac{\ell v_\theta(r_{\min})}{c_s} \log \frac{r}{r_{\min}} \right) \right\}. \end{aligned} \quad (\text{D2})$$

The names in/out and r/l are motivated from the direction in which these modes propagate once the time-dependence $e^{i\omega t}$ is added to them. $N_{\omega\ell}$ and $\tilde{N}_{\omega\ell}$ are two normalization constants. When $v_\theta(r_{\max}) \approx 0$, as in the case under consideration, $\tilde{N}_{\omega\ell}$ can be obtained by noticing that Bessel functions are exact solutions when $r \sim r_{\max}$, resulting in $\tilde{N}_{\omega\ell} = 1/\sqrt{4\pi\omega}$. This strategy does not work to obtain $N_{\omega\ell}$, because $v_\theta(r_{\min}) \neq 0$. We explain below how to compute this normalization constant.

For each mode (ω, ℓ) , we solve the radial differential equation (24) twice. On the one hand, we solve it using boundary data corresponding to the function $\varphi_l^{\text{in}}(r)$ and its first derivative at r_{\max} . We propagate the solution until r_{\min} where it becomes a linear combination of the two independent solutions $\varphi_r^{\text{in}}(r_{\min})$ and $\varphi_l^{\text{out}}(r_{\min})$. In other words, the asymptotic behavior of this solution is

$$\varphi_{\omega\ell}^{(1)}(r) = \begin{cases} a_{\omega\ell} \varphi_l^{\text{out}} + b_{\omega\ell} \varphi_r^{\text{in}} & r \rightarrow r_{\min} \\ \varphi_l^{\text{in}} & r \rightarrow r_{\max} \end{cases} \quad (\text{D3})$$

By fitting the numerical solution near r_{\min} to a linear combination of φ_l^{out} and φ_r^{in} we extract the coefficients $a_{\omega\ell}$ and $b_{\omega\ell}$. On the other hand, we repeat the calculation, this time with boundary data specified by $\varphi_r^{\text{out}}(r)$ at r_{\max} . The asymptotic form of the resulting solution is

$$\varphi_{\omega\ell}^{(2)}(r) = \begin{cases} c_{\omega\ell} \varphi_r^{\text{in}} + d_{\omega\ell} \varphi_l^{\text{out}} & r \rightarrow r_{\min} \\ \varphi_r^{\text{out}} & r \rightarrow r_{\max} \end{cases}, \quad (\text{D4})$$

from which we extract $c_{\omega\ell}$ and $d_{\omega\ell}$.

If the time and angular dependence $e^{-i\omega t} e^{i\ell\theta}$ is added to these radial functions, we obtain two ‘‘stationary’’ solutions to the wave equation. They are stationary in the sense that they do not describe propagating waves. Instead, they oscillate perpetually in time by virtue of their harmonic time dependence $e^{-i\omega t}$.

The trick to transform these stationary solutions into a dynamical scattering of waves is to integrate these solutions in a frequency range as follows:

$$\int_{j\epsilon}^{(j+1)\epsilon} d\omega e^{i\omega \frac{n}{\epsilon}} e^{-i\omega t} e^{i\ell\theta} \varphi_{\omega\ell}^{(i)}(r), \quad (\text{D5})$$

for $i = 1, 2$. In this equation, $j > 0$ and n are integers, and ϵ is a real number with dimensions of frequency. For $i = 1$, this function describes the following dynamical process

$$b_{\omega\ell} W_r^{\text{in}} + W_l^{\text{in}} \xrightarrow{\text{time}} a_{\omega\ell} W_l^{\text{out}}, \quad (\text{D6})$$

where $W_r^{\text{in}}, W_l^{\text{in}}$ and W_l^{out} are wave packets with mean frequency $\omega = (j + 1/2)\epsilon$ and bandwidth $\Delta\omega = \epsilon$. The integer n controls the region in spacetime in which these packets are supported. One can select ϵ to be small enough for the coefficients $a_{\omega\ell}$ and $b_{\omega\ell}$ not to change significantly with ω within the interval $\Delta\omega$. Similarly, the solution for $i = 2$ describes the scattering

$$c_{\omega\ell} W_r^{\text{in}} \xrightarrow{\text{time}} d_{\omega\ell} W_l^{\text{out}} + W_r^{\text{out}}. \quad (\text{D7})$$

The linearity of the dynamics allows us to take linear combinations of these two scattering processes to obtain information about another scattering process of interest. In particular, two appropriate linear combinations produce

$$W_r^{\text{in}} \xrightarrow{\text{time}} \frac{d_{\omega\ell}}{c_{\omega\ell}} W_l^{\text{out}} + \frac{1}{c_{\omega\ell}} \Phi_r^{\text{out}}, \quad (\text{D8})$$

and

$$W_l^{\text{in}} \xrightarrow{\text{time}} \left(a_{\omega\ell} - \frac{b_{\omega\ell} d_{\omega\ell}}{c_{\omega\ell}} \right) W_l^{\text{out}} + \frac{b_{\omega\ell}}{c_{\omega\ell}} W_r^{\text{out}}, \quad (\text{D9})$$

from which we can read the coefficients we are interested in

$$R_{\omega\ell} = \frac{d_{\omega\ell}}{c_{\omega\ell}}, \quad T_{\omega\ell} = \frac{1}{c_{\omega\ell}}, \quad t_{\omega\ell} = a_{\omega\ell} - \frac{b_{\omega\ell} d_{\omega\ell}}{c_{\omega\ell}} \quad \text{and} \quad r_{\omega\ell} = \frac{b_{\omega\ell}}{c_{\omega\ell}}. \quad (\text{D10})$$

This strategy allows us to determine the scattering coefficients $T_{\omega\ell}$, $R_{\omega\ell}$, $t_{\omega\ell}$ and $r_{\omega\ell}$ for each mode (ω, ℓ) , up to the normalization constant $N_{\omega\ell}$. This constant can be determined by demanding the scattering matrix \mathcal{S}_{SR} to be symplectic. Notice that this is a non-trivial requirement, since symplecticity of \mathcal{S}_{SR} imposes four constraints on $T_{\omega\ell}$, $R_{\omega\ell}$, $t_{\omega\ell}$ and $r_{\omega\ell}$ (Eqns. (A6), which correspond to four real conditions). We have checked that there is a unique value of $N_{\omega\ell}$ for which all four constraints are satisfied. Therefore, besides obtaining this normalization constant, our calculation actually provides a non-trivial test of symplecticity.

In table I we collect the result of our calculations, from which the plots shown in sections VI of this article can be reproduced.

$\ell = 1$				$\ell = 2$			
ω [μeV]	T	r = - R	t	ω [μeV]	T	r = - R	t
6.540	1.3410 + 0.2178i	0.0809 + 0.9161i	1.2821 - 0.4495i	13.34	1.1841 + 0.0743i	-0.1037 + 0.6300i	1.1455 + 0.3090i
7.063	1.3839 + 0.2507i	0.1415 + 0.9788i	1.2563 - 0.6324i	14.39	1.2189 + 0.1010i	-0.0403 + 0.7030i	1.2224 + 0.0389i
7.586	1.426 + 0.285i	0.2104 + 1.0351i	1.202 - 0.819i	15.43	1.2520 + 0.1346i	0.0362 + 0.7645i	1.2337 - 0.2525i
8.110	1.468 + 0.320i	0.2870 + 1.0836i	1.117 - 1.004i	16.48	1.2816 + 0.1760i	0.1229 + 0.8114i	1.1720 - 0.5476i
8.633	1.507 + 0.356i	0.3704 + 1.1228i	1.00 - 1.183i	17.53	1.3053 + 0.2260i	0.2158 + 0.8416i	1.0355 - 0.8262i
9.156	1.544 + 0.392i	0.4594 + 1.1514i	0.850 - 1.347i	18.57	1.3211 + 0.2850i	0.3107 + 0.8544i	0.8295 - 1.0671i
9.679	1.577 + 0.428i	0.5522 + 1.1682i	0.670 - 1.490i	19.62	1.3271 + 0.3533i	0.4034 + 0.8504i	0.5659 - 1.2513i
10.20	1.605 + 0.465i	0.6470 + 1.1724i	0.462 - 1.606i	20.67	1.3215 + 0.4304i	0.4904 + 0.8313i	0.2625 - 1.3648i
10.73	1.628 + 0.502i	0.7417 + 1.1636i	0.233 - 1.688i	21.71	1.3026 + 0.5156i	0.5687 + 0.7995i	-0.0597 - 1.3997i
11.25	1.646 + 0.539i	0.8338 + 1.1420i	-0.012 - 1.732i	22.76	1.2693 + 0.6074i	0.6366 + 0.7580i	-0.3789 - 1.3551i
11.77	1.657 + 0.577i	0.921 + 1.108i	-0.265 - 1.734i	23.81	1.2204 + 0.7039i	0.6934 + 0.7099i	-0.6751 - 1.2365i
12.30	1.660 + 0.615i	1.002 + 1.063i	-0.516 - 1.694i	24.85	1.1552 + 0.8026i	0.7390 + 0.6577i	-0.9312 - 1.0543i
12.82	1.657 + 0.653i	1.075 + 1.009i	-0.757 - 1.612i	25.90	1.0735 + 0.9009i	0.7741 + 0.6040i	-1.1349 - 0.8222i
13.34	1.646 + 0.693i	1.138 + 0.946i	-0.982 - 1.492i	26.94	0.9752 + 0.9957i	0.7996 + 0.5504i	-1.2782 - 0.5555i
13.86	1.628 + 0.733i	1.191 + 0.878i	-1.182 - 1.338i	27.99	0.8607 + 1.0838i	0.8167 + 0.4985i	-1.3574 - 0.2700i
14.39	1.603 + 0.775i	1.233 + 0.806i	-1.353 - 1.157i	29.04	0.7312 + 1.1621i	0.8267 + 0.4490i	-1.3728 + 0.0193i
14.91	1.570 + 0.817i	1.264 + 0.731i	-1.491 - 0.954i	30.08	0.5880 + 1.2274i	0.8307 + 0.4026i	-1.3278 + 0.2989i
15.43	1.531 + 0.860i	1.285 + 0.657i	-1.594 - 0.737i	31.13	0.4331 + 1.2769i	0.8299 + 0.3597i	-1.2279 + 0.5571i
15.96	1.485 + 0.903i	1.297 + 0.583i	-1.662 - 0.512i	32.18	0.2689 + 1.3080i	0.8251 + 0.3202i	-1.0809 + 0.7843i
16.48	1.434 + 0.947i	1.3003 + 0.5120i	-1.695 - 0.285i	33.22	0.0984 + 1.3187i	0.8172 + 0.2841i	-0.8953 + 0.9731i
17.00	1.377 + 0.990i	1.2959 + 0.4439i	-1.695 - 0.062i	34.27	-0.0752 + 1.3071i	0.8068 + 0.2514i	-0.6807 + 1.1184i
17.53	1.315 + 1.032i	1.2849 + 0.3795i	-1.665 + 0.152i	35.32	-0.2483 + 1.2724i	0.7946 + 0.2218i	-0.4467 + 1.2170i
18.05	1.249 + 1.073i	1.2683 + 0.3193i	-1.608 + 0.354i	36.36	-0.4173 + 1.2140i	0.7809 + 0.1952i	-0.2029 + 1.2676i

$\ell = 3$				$\ell = 4$			
ω [μeV]	T	r = - R	t	ω [μeV]	T	r = - R	t
19.62	1.1085 + 0.0208i	-0.2272 + 0.4214i	0.6264 + 0.9148i	26.68	1.0795 + 0.0172i	-0.3017 + 0.2730i	-0.0905 + 1.0758i
21.19	1.1390 + 0.0352i	-0.1721 + 0.5185i	0.9341 + 0.6527i	28.78	1.1089 + 0.0287i	-0.2626 + 0.4018i	0.4714 + 1.0041i
22.76	1.1686 + 0.0585i	-0.0910 + 0.6007i	1.1335 + 0.2905i	30.87	1.1372 + 0.0498i	-0.1757 + 0.5147i	0.9302 + 0.6562i
24.33	1.1943 + 0.0937i	0.0092 + 0.6596i	1.1912 - 0.1271i	32.96	1.1596 + 0.0865i	-0.0532 + 0.5910i	1.1564 + 0.1219i
25.90	1.2125 + 0.1440i	0.1193 + 0.6905i	1.0939 - 0.5426i	35.05	1.1706 + 0.1450i	0.0841 + 0.6199i	1.0897 - 0.4515i
27.47	1.2198 + 0.2117i	0.2290 + 0.6929i	0.8534 - 0.8969i	37.15	1.1651 + 0.2295i	0.2141 + 0.6036i	0.7601 - 0.9123i
29.04	1.2124 + 0.2974i	0.3296 + 0.6706i	0.5051 - 1.1416i	39.24	1.1375 + 0.3407i	0.3215 + 0.5537i	0.2681 - 1.1568i
30.61	1.1868 + 0.4003i	0.4153 + 0.6296i	0.0992 - 1.2486i	41.33	1.0817 + 0.4748i	0.4001 + 0.4851i	-0.2602 - 1.1523i
32.18	1.1396 + 0.5173i	0.4834 + 0.5767i	-0.3103 - 1.2124i	43.43	0.9912 + 0.6239i	0.4508 + 0.4105i	-0.7138 - 0.9286i
33.75	1.0674 + 0.6436i	0.5340 + 0.5181i	-0.6755 - 1.0475i	45.52	0.8609 + 0.7761i	0.4786 + 0.3385i	-1.0186 - 0.5531i
35.32	0.9677 + 0.7729i	0.5688 + 0.4587i	-0.9604 - 0.7820i	47.61	0.6881 + 0.9169i	0.4891 + 0.2737i	-1.1414 - 0.1067i
36.89	0.8392 + 0.8974i	0.5903 + 0.4016i	-1.1429 - 0.4510i	49.70	0.4741 + 1.0299i	0.4878 + 0.2179i	-1.0835 + 0.3341i
38.46	0.6820 + 1.0090i	0.6013 + 0.3488i	-1.2144 - 0.0911i	51.80	0.2253 + 1.0991i	0.4789 + 0.1714i	-0.8717 + 0.7063i
40.02	0.4983 + 1.0989i	0.6042 + 0.3012i	-1.1775 + 0.2633i	53.89	-0.0462 + 1.1100i	0.4653 + 0.1334i	-0.5491 + 0.9658i
41.59	0.2922 + 1.1590i	0.6011 + 0.2593i	-1.0435 + 0.5829i	55.98	-0.3235 + 1.0525i	0.4493 + 0.1028i	-0.1666 + 1.0884i
43.16	0.0701 + 1.1821i	0.5939 + 0.2228i	-0.8302 + 0.8445i	58.08	-0.5857 + 0.9219i	0.4322 + 0.0785i	0.2240 + 1.0690i
44.73	-0.1596 + 1.1627i	0.5838 + 0.1913i	-0.5593 + 1.0318i	60.17	-0.8099 + 0.7210i	0.4150 + 0.0594i	0.5752 + 0.9192i
46.30	-0.3871 + 1.0973i	0.5718 + 0.1643i	-0.2546 + 1.1354i	62.26	-0.9741 + 0.4602i	0.3983 + 0.0446i	0.8484 + 0.6640i
47.87	-0.6014 + 0.9851i	0.5586 + 0.1415i	0.0601 + 1.1526i	64.35	-1.0594 + 0.1578i	0.3823 + 0.0332i	1.0164 + 0.3379i
49.44	-0.7911 + 0.8282i	0.5449 + 0.1221i	0.3620 + 1.0866i	66.45	-1.0533 - 0.1615i	0.3672 + 0.0246i	1.0654 - 0.0195i
51.01	-0.9456 + 0.6317i	0.5309 + 0.1058i	0.6311 + 0.9460i	68.54	-0.9514 - 0.4689i	0.3532 + 0.0183i	0.9949 - 0.3678i
52.58	-1.0550 + 0.4035i	0.5170 + 0.0922i	0.8505 + 0.7433i	70.63	-0.7593 - 0.7344i	0.3401 + 0.0139i	0.8168 - 0.6699i
54.15	-1.1118 + 0.1541i	0.5033 + 0.0808i	1.0076 + 0.4945i	72.72	-0.4922 - 0.9303i	0.3279 + 0.0110i	0.5535 - 0.8952i

TABLE I. Numerical data for the scattering coefficients, obtained as described above, with the velocity profile (27), with values $\alpha_1 = 2c_s$, $c_s = 0.7\mu\text{m ps}^{-1}$, $\alpha_2 = 0.3\mu\text{m}^{-1}$ and $\alpha_3 = 45\mu\text{m}$.